Investigating nano-precipitation in a V-containing HSLA steel using small angle neutron scattering

Y. Q. Wang[a, b], S. J. Clark[c], V. Janik[c, d], R. K. Heenan[e], D. Alba Venero[e], K. Yan[a, b], D. G. McCartney[b, f], S. Sridhar[c, g], P. D. Lee[a, b]

[a] *School of Materials, University of Manchester, Manchester, M13 9PL, UK*

[b] *Research Complex at Harwell, Rutherford Appleton Laboratory, Harwell, OX11 0FA, Oxfordshire, UK*

[c] *WMG, University of Warwick, Coventry, CV4 7AL, UK*

[d] *Faculty Research Centre for Manufacturing and Materials Engineering, Coventry University, Coventry, CV1 5FB, UK,*

[e] *Rutherford Appleton Laboratory, Didcot, Oxfordshire, OX11 0QX, UK*

[f] *, Advanced Materials Group, University of Nottingham, Nottingham, NG7 2RD, UK*

[g] *, George S. Ansell Department of Metallurgical and Materials Engineering, Colorado School of Mines, Golden, CO 80401, USA*

Abstract

Interphase precipitation (IPP) of nanoscale carbides in a vanadium-containing high-strength low-alloy steel has been investigated. Small angle neutron scattering (SANS) and transmission electron microscopy (TEM) were employed to characterize the precipitates and their size distributions in Fe-0.047C-0.2V-1.6Mn (in wt.%) alloy samples which had been austenitized, isothermally transformed at 700 °C for between 3 and 600 min and water quenched. TEM confirms that, following heat treatment, rows of vanadium-containing nanoscale interphase precipitates were present. Model-independent analysis of the nuclear SANS signal and model fitting calculations, using oblate spheroid and disc-shapes, were performed. The major axis diameter increased from 18 nm after 3 min to 35 nm after 600 min. Precipitate volume percent increased from 0.09 to 0.22 vol% over the same period and number density fell from 2×10^{21} to $5 \times 10^{20} \, \text{m}^{-3}$. A limited number of measurements of precipitate maximum diameters from TEM images showed the mean value increased from

28 8 nm after 5 min to 28 nm after 600 min which is in reasonable agreement with the SANS

29 data.

30 Key Words: Microalloyed steel, Precipitation, Small angle scattering, Transmission electron

31 microscopy

1. Introduction

33 High-strength, low-alloy (HSLA) steels which contain typically 0.05 to 0.15 wt%C, up to 2

34 wt%Mn and small (microalloy) additions of elements Mo, Nb, Ti and V (all usually <0.2wt%)

35 have been in use as rolled sheet for automotive products for a number of years [1-6]. These

36 small additions can form carbo-nitride (MX) (M =Mo,Nb,V,Ti and X = C,N) precipitates

37 having the B1 (Fm3m) NaCl-type, FCC structure within the BCC ferrite (α-Fe) matrix [3].

38 However, there is a significant need to reduce the weight of automobiles in order to improve

39 vehicle efficiency and achieve reduced fuel consumption and emissions. At the same time,

40 passenger safety must not be compromised and so there is a growing demand from the

41 automotive industry for highly formable steels with increased strength [7, 8]. This demand

42 has led to intensive research and a growth in the production of steels that offer improved

43 property combinations. These are termed advanced high strength steels (AHSS). The major

44 difference between HSLA steels and AHSS is that the former have predominantly ferritic

45 microstructures with a small volume fraction of microalloy carbonitride precipitates whereas

46 the latter comprise dual phase (DP) steels (e.g. ferrite plus martensite) and steels that exhibit

47 phenomena such as transformation induced and twinning induced plasticity. Nonetheless,

48 there are some important differences between the mechanical behaviours of DP steels and

49 predominantly single phase steels which are precipitation strengthened [9].

50 For example, it has been reported that the local elongation of DP steels, such as is required

51 for hole expansion operations in manufacturing, is lacking in DP alloys. In response to this

52 need, Funakawa et al.[10] reported the development of a new type of hot rolled steel that is

53 based on a composition which gives rise to a ferrite matrix with nanometre-sized microalloy

54   carbides. The latter are formed via the well-known interphase precipitation mechanism in

55   which rows and sheets of nanometre scale MX precipitates form at a moving α/γ interface

56   during either isothermal transformation or continuous cooling and their very fine scale leads

57   to a large precipitation hardening effect [2, 10-19]. The steel composition and processing

58   conditions need to be carefully selected to avoid the formation of pearlite or cementite which

59   would degrade formability [10].

60   In this context, there has been renewed interest in the topic of interphase precipitation (IPP),

61   first investigated more than 40 years ago, as a means of introducing precipitates that are

62   typically 5-15 nm in diameter, with rows that are ~ 30 to 50 nm apart. Vanadium carbide is

63   often selected as an interphase precipitate because the solubility product of VC in austenite is

64   much larger than that of TiC or NbC [20]. Therefore, it has little tendency to precipitate in the

65   γ phase but instead precipitates during cooling so that a relatively large amount of

66   precipitation occurs in the α-ferrite. However, maintaining a fine precipitate size during steel

67   processing (i.e. prevention of precipitate coarsening by Ostwald ripening) is crucial to

68   achieving a sufficiently large precipitation hardening effect in the final product. Vanadium

69   carbide has a relatively high coarsening rate and consequently, significant attention has also

70   been given to the investigation of Ti and Ti-Mo-containing steels. Both systems exhibit IPP

71   but it has been found that the coarsening of carbide precipitates is significantly retarded in Ti-

72   Mo alloys [14, 21-25].

73   Previous studies of IPP have included topics such as the effect of transformation temperature

74   [11, 15, 26], time [27], cooling rate [16, 28-30], orientation relationship [15, 31-35], hot

75   deformation [17, 36] as well as the addition of Mo [10, 14, 21-25] on precipitate composition,

76   size, morphology and number density. The majority of these prior studies have used

77   transmission electron microscopy (TEM) to characterise the precipitates [14, 18, 19, 22, 37,

78   38]. More recently atom probe tomography (APT) [15, 35, 39, 40] has been employed to

79   directly measure the composition, morphology, and size of individual precipitates. However,

80   obtaining reliable statistical data on particle size distributions, chemical composition,

81   morphology and volume fractions following IPP is a particular challenge as IPP typically

82   occurs inhomogeneously [15, 35, 41]. TEM and APT both have a limited capability to

83   analyse statistically significant numbers of precipitates efficiently which limits our ability to

84   predict mechanical properties via models of precipitate - dislocation interactions. The lack of

85   representative data on precipitates from significant volumes of bulk material, including

86   factors such as size and spacing, also restricts the development of new and improved models

87   of interphase precipitation [18, 42-49]. Improved, statistically significant, data on the size and

88   distribution of interphase precipitates from bulk samples are thus needed.

89   Small angle scattering techniques based on neutrons or X-rays are potentially suitable for

90   acquiring bulk-scale, statistically sound data on fine scale IP precipitates of the MX type in

91   HSLA steels. Small angle neutron scattering (SANS) is generally preferred and over the past

92   twenty years, there has been a growing interest in its use to measure the size, size distribution

93   and volume fraction of nanoscale precipitates in various types of steel. This has included

94   studies at room temperature on strip cast low carbon steels [37, 50, 51], maraging and

95   martensitic steels [52, 53], Ti and Nb-containing microalloyed steels [54-57], Nb-containing

96   pipeline steels [58] and NbC precipitation in the austenite phase [59]. Although Oba et al. [60]

97   investigated IPP in a vanadium microalloyed steel, this was a medium-carbon grade and

98   quantitative data on IPP in low-carbon, V- microalloyed steels have not apparently been

99   reported.

100   The overall purpose of the present work was to use SANS to quantitatively analyze the size

101   and volume fraction of IP precipitates and to investigate the changes occurring during

102   isothermal transformation. A steel of composition Fe-0.047C-0.2V-1.6Mn (in wt.%) was

103   selected for the present investigation because V is the most soluble of the microalloying

104   elements in austenite (γ) at high temperature and it does not readily precipitate in the γ-phase

105 during cooling making it a very suitable addition for the formation of IP precipitates. In the

106 present study, we measured precipitate characteristics from both the magnetic and the nuclear

107 scattering signals and correlated the measurements with electron microscope observations

108 and microhardness data. The results will aid modelling of precipitation strengthening and in

109 the selection of suitable thermomechanical processing schedules for controlled IPP, with a

110 SANS methodology extendable to a wider range of ferromagnetic alloys.

111 2. **Materials and methods**

112 **2.1 Materials**

113 A V-containing, microalloyed low-carbon steel provided by Tata Steel Europe was employed.

114 The composition of the alloy, as determined by chemical analysis, is given in Table 1. The

115 alloy was prepared by vacuum induction melting and cast into ingots with dimensions of 350

116 x 105 x 100 mm. These ingots were forged at approximately 1250 °C to a final thickness of

117 35 mm (i.e. a reduction of 65 %) and air cooled. To ensure that the thermomechanical

118 processing was relevant to that employed in industrial operations, the additional 2-3 day

119 homogenization stage at high temperature used in some prior studies on other alloys, was not

120 applied. Six samples (with dimensions of $30 \times 10 \times 6$ mm) were machined from the forgings

121 and austenitized in a salt bath at 1150 °C for 5 min. One of the samples was water quenched

122 directly from 1150 °C. The remaining samples were transferred directly to another salt bath

123 and held at 700 °C for periods in the range 3 min to 600 min and water quenched (see

124 Supplementary Data). Approximately 0.5 mm was removed from the surfaces prior to SANS

125 analysis or further sample preparation for microscopy.

126 **2.2 Materials characterization**

127 Samples were sectioned and metallographically prepared by the normal methods. Scanning

128 electron microscopy (SEM) was conducted using an FEI Quanta 650 FEG-SEM operated at a

129   voltage of 20 kV. Specimens were given a final polish with a colloidal silica suspension (OPS)

130   and etched with 2% Nital.

131   For examination in the transmission electron microscope (TEM), samples were prepared by

132   mechanical grinding/polishing to 50 μm thickness and then twin-jet electro-polished in a

133   solution of 10 vol.% $HClO_4$ mixed with 90 vol.% CH_3COOH at approximately -15°C. TEM

134   observations were performed using a JEOL 2100 scanning TEM operating at 200 kV

135   equipped with 80 mm^2 silicon drift EDS detector (SDD) Oxford Instruments X-Max; aperture

136   size 5 nm was used for STEM-EDS acquisition. Additionally, to examine in more detail the

137   sample heat-treated for 600 min, an FEG-TEM FEI Talos F200X operating at 200 kV with

138   four integrated Super-X SDD EDS detectors at a detection angle of 0.9 srad was used for

139   high resolution imaging and elemental mapping of vanadium. In this case, a modified focused

140   ion beam (FIB) lift-out method was used to prepare foils ~120 nm in thickness. The modified

141   FIB preparation procedure involved an initial standard sample lift out preparation with 25 kV

142   Ga-ions followed by a final low energy Ga-ion milling at 500 V and at an angle of 12° on

143   both sides of the TEM foil sample [61]. This was designed to minimise the level of ion-

144   induced damage due to surface re-deposition, amorphisation and implantation and to allow

145   accurate observation of nano-scale features.

146   The average precipitate diameters in the samples aged for 5 min and for 600 min were

147   measured from bright field TEM images and STEM-EDS maps by exporting them to ImageJ

148   software [62]. Assuming that all precipitates have either oblate spheroid or disc-shaped

149   morphologies an individual particle diameter was calculated as being equal to the calibrated

150   diameter of the major axis (long axis) on the image plane. For each ageing condition, a

151   minimum of 300 precipitates, both random and interphase, were analysed from a total of 20

152   TEM images.

The microhardness (Hv) of isothermally transformed samples was measured using a Wilson VH3100 microhardness tester with a load of 0.1 kgf. In partially transformed samples, indents were placed only within the ferrite grains. The mean value of 25 measurements is reported and the error is given as one standard deviation.

2.3 SANS experiment method

Small angle neutron scattering (SANS) experiments were performed on the SANS2d beamline at the ISIS Pulsed Neutron Source, UK [63]. A schematic of the experimental setup is shown in Fig. 1. Small angle scattering arises from nanoscale precipitates embedded in the ferritic matrix (as shown in Fig. 1a and 1b) as well as larger scale structural features. A magnetic field of 1.5 T was applied in a horizontal direction parallel to the sample surface (i.e. perpendicular to the neutron beam) sufficient to saturate the α-Fe matrix and suppress multiple scattering. Polychromatic neutrons (λ=1.7 to 16.5 Å) were used but only wavelengths in the range of 4.7 to 16.5 Å were selected for data analysis in order to avoid multi-Bragg diffraction [64-66]. Samples of approximately 10 mm $\times$ 10 mm $\times$ ~1 mm (thickness) were polished to 1 μm diamond surface finish and exposed for 60 min to a neutron beam of 8 mm diameter. The detector configuration gave a small angle scattering vector (q) range of 0.004 to 0.3 Å^{-1}, where $q= 4\pi sin\theta/\lambda$ and the scattering angle is 2θ. Absolute SANS intensities were obtained using standard procedures [5, 67]. Nuclear and "nuclear plus magnetic" scattering cross-sections were obtained by partial azimuthal averaging in 30° sectors around the transmitted beam as shown in Figure 1(c) leading to one-dimensional plots of scattering intensity, I, versus q (Figure 1(d)). (Further details in Supplementary Data).

3. SANS data reduction and analysis method

If the precipitates are assumed to be non-interacting particles then the SANS scattering intensity, I, of the particle dispersion is given by

178
$$I(q) = (\Delta\rho)^2 \int_0^\infty N(r)V(r)^2 F(q,r)^2 \, dr \qquad (1)$$

179 where $\Delta\rho$ is the difference in the scattering length densities of the particle and the matrix,

180 $N(r)dr$ is the number density of particles with size between r and $r+dr$, $V(r)$ is the volume of

181 a particle of size r and $F(q,r)$ is the form factor for the particles and q is the scattering vector

182 [66, 68, 69].

183 Neutron scattering contrast has both a magnetic, $\Delta\rho_{mag}$, and a nuclear, $\Delta\rho_{nuc}$, contributions. In

184 a field that magnetizes the matrix to saturation, $I(q)$ depends on the angle ϕ between the

185 scattering vector and the magnetic field. Thus $\Delta\rho$ in eqn. 1 can be written as

186
$$(\Delta\rho)^2 = (\Delta\rho_{nuc})^2 + (\Delta\rho_{mag})^2 \sin^2\phi \qquad (2)$$

187 Fig. 1c shows an example of a two dimensional detector image arising from this effect. The

188 nuclear scattering intensity is measured along $\phi = 0°$ and the sum of nuclear and magnetic

189 scattering along $\phi = 90°$. To produce one-dimensional scattering profiles (Fig. 1(d)) we

190 employed azimuthal data integration from $-15 < \phi < +15°$ to determine nuclear scattering and

191 between $75 < \phi < +105°$ to find nuclear plus magnetic scattering.

192 When the matrix is magnetized to saturation, and the chemical size of the precipitates is the

193 same as their magnetic size, the ratio $R(q)$ depends on their chemical composition through the

194 dependence of $\Delta\rho_{nuc}$ on precipitate chemistry.

195
$$R(q) = \frac{I_{mag}(q)}{I_{nuc}(q)} = \left(\frac{\Delta\rho_{mag}}{\Delta\rho_{nuc}}\right)^2 \qquad (3)$$

196 If all precipitates have the same composition then $R(q)$ is constant. However, $R(q)$ will vary if

197 either there is more than one type of precipitate present of differing size or the precipitate

198 composition is size dependent [54].

199 Our model independent analysis (assuming disc-shaped IP precipitates) of particles is based

200 on the Guinier, Kratky and Porod representations of the absolute scattering intensity data and

201 follows standard methods [68-70].

202   A radius of gyration, R_{g1}, is calculated from the Guinier plot (which takes the form of ln(*I*) *vs*

203   q^2) using a self-consistent method with $1 < qR_{g1} < 2$.

204   For a distribution of monodisperse thin discs of thickness, *T*, and radius, *R*, the relationship

205   between *T*, *R* and R_{g1} is given by [70]

$$R_{g1}^2 = \frac{T^2}{12} + \frac{R^2}{2} \tag{4}$$

207   A second Guinier plot of $\ln[q^2(I)]$ vs q^2 is known to give a radius of gyration, R_{g2}, that is

208   related to the thickness, *T*, of a disc.

$$R_{g2} = \left(\frac{T^2}{12}\right)^{1/2} \tag{5}$$

210   However, for polydisperse distributions there is not a simple relationship between R_{g1}, R_{g2}

211   and mean particle dimensions as discussed in detail by Deschamps and De Geuser [69].

212   In the Kratky plot, Iq^2 is plotted versus *q* and a characteristic particle size, R_{max},(the "pseudo

213   Guinier radius",) can be determined from the maximum, q_{max}, in the plot [69].

$$R_{max} = \frac{\sqrt{3}}{q_{max}} \tag{6}$$

215   The volume fraction of precipitate, f_v, in a dilute incompressible two-phase system is also

216   obtained from the Kratky plot. The integrated small angle scattering, Q, (i.e. the Porod

217   invariant) is given by

$$Q = \int_0^\infty I(q)\,q^2\,dq = 2\pi^2 \left(\rho_\rho - \rho_m\right)^2 f_v \left(1 - f_v\right) \tag{7}$$

219   where ρ_p and ρ_m are the scattering length densities (either nuclear or magnetic) of precipitate

220   and matrix respectively. The *q*-range for integration was extrapolated to 10^{-5} Å^{-1} for low *q*

221   and 10 Å^{-1} for high *q* with the Guinier equation and the Porod law respectively as

222   recommended in reference [66]. Thus f_v can be found using the data in Supplementary Note 3.

223   A model fitting analysis was also carried out based on physical understanding from the

224   model-independent analysis and using the SasView software program [71]. Two kinds of

225   form factor fitting functions were investigated based on precipitates being assumed to be

226   either disc or an oblate ellipsoid of revolution shape (i.e. an oblate spheroid).

227   In the case of a disc, the form factor is given by

228     $$F_{disc}(q, R, T) = \frac{2J_1(qRsin\alpha)}{qRsin\alpha} \frac{sin(qTcos\alpha)}{qTcos\alpha} \tag{8}$$

229   where α is the angle between the axis of the thin disc, q the scattering vector, T the thickness

230   of the disc and R is the radius. J_1 is a first order Bessel function.

231   For the ellipsoidal shape, the form factor becomes

232     $$F_{ellipsoid}(q, a, b) = 3 \frac{sin[qr(a,b,\alpha)] - cos[qr(a,b,\alpha)]}{(qR)^3} \tag{9}$$

233     $$\text{where } r(a, b, \alpha) = (asin^2\alpha + bcos^2\alpha)^{0.5} \tag{10}$$

234   α is the angle between the axis of the ellipsoid and q, where b and a are the radii along and

235   perpendicular to the rotation axis of the ellipsoid respectively; b is referred to as the polar

236   axis and a is the equatorial axis.

237

4. Results and Discussion

4.1. Microstructural characterization

240   The SEM image of Fig. 2a shows the microstructure of the water quenched alloy which is

241   seen to consist of acicular units, irregularly shaped laths and fine scale precipitates. These

242   features indicate the formation of an auto-tempered martensite and lower bainite. Figs. 2(b)-(f)

243   show the microstructure of samples transformed at 700 °C followed by water quenching.

244   Regions of bainite, which formed from untransformed austenite that was present at the time

245 of quenching, are evident in Figs. 2(b)-(d). However, bainite is not visible in the samples

246 transformed for 300 min and 600 min (Figs. 2(e) and (f)), indicating that transformation from

247 austenite was complete prior to 300 min of isothermal holding. In the SEM image of Fig. 2(f),

248 IP precipitates are visible within the ferrite grains. These precipitates can be resolved in the

249 SEM because they have coarsened as a result of the long holding time at 700 °C.

250 Bright field TEM images of the samples transformed at 700°C for 5 min and 600 min

251 respectively are shown in Figs. 3(a) and 3(b). For both transformation times, planar rows of

252 carbide precipitates are observed which indicate that they have most probably been formed

253 by interphase precipitation.

254 The morphology of the precipitates cannot be fully determined from these two images but is

255 consistent with either a rod or disc-shape. Previous work has reported that IP precipitated

256 vanadium carbides are not spherical but mostly elongated along the $(001)_{VC}$ plane to give an

257 oblate spheroid (i.e. disc-shaped) morphology. This occurs because the $(001)_{VC}$ plane is a

258 habit plane of VC and parallel to (001) plane in the ferrite [19, 72]. Therefore, in this study

259 we assume that the vanadium carbides also exhibit such a morphology. Figs. 3(c) and 3(d)

260 show representative high resolution TEM lattice images of the carbide precipitates in the

261 sample held for 600 min. The long axis diameter of the precipitates are around 21 nm to

262 28 nm. The EDX map (Fig. 3(e)) confirms the precipitates are V-rich.

263 Precipitate size measurements, performed as described in section 2.2 on TEM images and

264 EDX maps, give a mean value for the long axis carbide diameter. After 5 min ageing, this

265 was found to be 7.8±3.6 nm and after 600 min ageing it was 27.8±8.0 nm (where the errors

266 correspond to the standard deviation in the data). The long axis measurement is consistent

267 with the HR-TEM lattice image and the change in long axis diameter with ageing time

268 indicates a significant coarsening effect.

269

270 **4.2 Interpretation of small angle neutron scattering measurements**

One-dimensional plots of intensity versus scattering vector extracted from the SANS data for the water quenched and isothermally transformed (3, 60 and 300 min) alloys are shown in Figs. 4(a)-(d) respectively. In the water quenched sample, only the nuclear signal closely follows a q^{-4} variation (i.e. the Porod Law) over the entire q-range until the background level is reached at $q>0.1$ Å^{-1}. This shows that the principal contribution to nuclear scattering is from the interface between scattering particles and the matrix where the particles are large scale features typically $> 2\pi/q_{min}$ (approx. 150 nm). These will typically be alloy carbides, nitrides or sulphides formed during steel manufacture. The iron carbides present in the bainitic regions of the quenched alloy (Fig. 2(a)) make negligible contribution to the nuclear scattering pattern because of their small contrast factor (See Supplementary Data). If nanoscale VC precipitates had formed they would contribute strongly to the nuclear signal due to their large contrast factor and so the q^{-4} behaviour of the nuclear signal indicates that there is no detectable nanoscale VC present following austenitization and quenching. However, the magnetic scattering signal deviates significantly from a q^{-4} behaviour over the range $0.004<q<0.05$ Å^{-1} because magnetic scattering is significant from iron carbide precipitates (they are not ferromagnetic and behave as magnetic "holes" in the matrix).

The SANS results obtained from the isothermally transformed samples which were water quenched following transformation times of 3, 60, and 300 min are also shown in Fig. 4. In Fig. 4(b) both magnetic and nuclear scattering intensities deviate from a q^{-4} Porod-type behaviour. In the case of the nuclear signal, the deviation at $q \sim 0.01$ Å^{-1} arises from the formation of nanoscale ($d \leq 50$ nm) VC precipitates, formed during the isothermal hold as seen in the TEM images of Figs. 3. The magnetic signal shows a different behaviour to the nuclear one due to the presence of residual islands of transformed austenite (i.e. bainite) (Figs. 2(b)-2(d)) which contain iron carbides. The magnetic signal thus has contributions from both the nanoscale VC and the somewhat larger iron carbide phases giving rise to a deviation from q^{-4} behaviour at lower values of the scattering vector q (larger values of particle size). Fig. 4(c)

shows similar features to Fig. 4(b) but the difference between nuclear and magnetic signals is diminished due to the reduced fraction of bainite in the microstructure following 60 min transformation followed by quenching, giving a reduced quantity of iron carbide compared to the shorter ageing time. The magnitude of the nuclear signal is evidently increased as a result of a greater phase fraction of VC and the signal covers a larger range of scattering vector, q. Following 60 min transformation, the nuclear and magnetic signals are similar, consistent with the very small volume fraction of bainite seen in Fig. 2(d). In Fig. 4(d), the nuclear and magnetic signals have a similar magnitude over the entire q range following 300 min transformation. Two factors contribute to this. First, the nuclear and magnetic contrast factors of VC are similar (Supplementary Data). Secondly, isothermal transformation of austenite to ferrite was complete following a 300 min hold and hence there was no additional scattering contribution from iron carbides. Thus the large overall scattering signal above the Porod background is due to the nanoscale VC precipitates as seen in the TEM images of Fig. 3. The 1-D pattern for the sample transformed for 600 min is not shown but it has very similar features to Fig. 4(d) and is given in Supplementary Data.

Figure 5 shows the ratio of magnetic to nuclear scattering ($R(q)$ versus q, equation 3) for the water quenched and isothermally transformed samples. For the water quenched sample, the plot has a maximum value of 10.5 at $q \sim 0.04\text{Å}$. This implies the magnetic scattering signal was raised by iron carbide particles ranging in size from 15 to 150 nm. The dependence of $R(q)$ on q decreased significantly with increasing transformation time and the maximum value of $R(q)$ shifted to smaller q values indicating an increase in the size of the iron carbides in the bainite formed on quenching as well as the formation of a second type of precipitate with a much lower $R(q)$ value, presumably the vanadium carbide precipitates.

The austenite to ferrite transformation was completed in the samples transformed for 300 and 600 min and the corresponding values of $R(q)$ are almost independent of q and close to 1. This is consistent with the formation of a single V-containing carbide, the composition of

323 which is independent of size. However, the mean value decreases slightly with transformation

324 time (Table 2), which could be due to the mean carbide composition changing with time.

325

326 **4.3 Determination of precipitate characteristics and the effect of transformation time**

327 Further analysis of the changing VC volume fraction, size and size distribution during

328 isothermal transformation is based on the 1-D nuclear data shown in Fig. 4, with the removal

329 of (i) the effect of Porod Law scattering (large particles) and (ii) the incoherent background

330 [66]. Figure 6(a) shows the intensity, I, versus scattering vector, q, the Kratky representation

331 (Iq^2 versus q) is shown in Fig. 6(b), Fig. 6(c) is the first Guinier representation ($ln(I)$ versus q^2)

332 and Fig. 6(d) is the second Guinier representation ($ln(q^2I)$ vs q^2).

333 *Principal features of the I(q) versus q plots*

334 It is clear from Fig. 6(a) that the I versus q^n power law exponents depend on the q range. At

335 low q (region I) and high q (region III) ranges, the exponent is found to have values of 0 and -

336 4 respectively. The exponent zero corresponds to the Guinier regime which probes real space

337 regions of size q^{-1}; ie regions >> precipitate sizes [73]. The exponent -4 relates to the Porod

338 regime which probes the interfaces between the precipitate and the matrix. The scattering

339 intensity is related to the precipitate surface area per unit volume. The intermediate q region

340 (II) follows an exponent of approximately -2 as indicated in Fig. 6a. In this regime, the slope

341 is related to the shape of the precipitate and q^{-2} indicates that the precipitates are thin discs or

342 oblate spheroids [74] and so this slope is consistent with the precipitate morphology observed

343 in the TEM images (Fig. 3).

344

345 *Precipitate size and precipitate volume fraction calculated from Kratky plot*

346 The Kratky plots of Iq^2 versus q (where I is the nuclear intensity) for samples transformed for

347 different times are shown in Fig. 6(b). These plots provide a visual indication of volume

348 fraction and size of the VC precipitates. The precipitate volume fraction is calculated from

14

349   the area under the Kratky plot (equation 7) whilst, q_{max} (equation 6) provides an estimate of

350   the particle size which is termed the pseudo-Guinier radius, R_{max}. Numerical curve fitting was

351   used to find q_{max} and R_{max} values. The values obtained for volume fraction, f_v, and R_{max} are

352   listed in Table 2 and it is evident that both of these increase with transformation time. The

353   different sets of values for f_v arise from the different assumptions made in applying Eq. (7). In

354   one case, it was assumed that the precipitate had the stoichiometric VC composition giving a

355   constant nuclear contrast factor in the calculation of f_v. In the other case, a mean $R(q)$ value

356   (taken from Fig. 5) was used to calculate the nuclear contrast factor on the assumption of a

357   constant magnetic contrast factor (see Supplementary Data). It was only possible to perform

358   mean $R(q)$ estimates for the fully transformed samples i.e. the 300 and 600 min

359   transformation times. The values obtained from the constant nuclear contrast calculation

360   probably represent an upper-bound value for f_v.

361   Considering now the interpretation of the pseudo-Guinier radius R_{max}, it is shown in reference

362   [69] that the relationship between R_{max} and the mean particle radius depends on both the

363   value of the dispersion parameter and also on the aspect ratio of the precipitate. Despite this

364   limitation, the increase in R_{max} with transformation time shown in Table 2 suggests a marked

365   coarsening behaviour of the precipitate population with the transformation time when held at

366   700 °C.

367

368   *Precipitate size calculated from Guinier plot*

369   Plots of the Guinier equations used to derive R_{g1} (*ln(I) vs q^2*) and R_{g2} (*ln(q^2(I) vs q^2*) from the

370   gradients are displayed in Figs. 6(c) and (d) respectively and values of R_{g1} and R_{g2} are listed

371   in Table 2. In both cases, self-consistent methods were applied for the boundaries of the

372   linear gradient fitting [69]. Clearly, these parameters increase with transformation time,

373   which correlates with the change in R_{max} and indicate a progressive increase in precipitate

374   dimensions.

375 The limitations of the classical Guinier approach in calculating average particle dimensions

376 for polydisperse systems are well documented [69]. Nonetheless, estimates of disc radius, R,

377 and thickness, T, of the assumed disc shaped VC precipitates based on the Guinier approach

378 can give valuable size data, recognizing that they represent particle ensemble information,

379 and are given in Table 3 as calculated using equations (4) and (5). These show that both

380 radius and thickness increase significantly and the aspect ratio of the particles is seen to be

381 around 3-4 and changes little with transformation time. The Guinier radii after 5 min and

382 600 min ageing time of 11.6 nm and 21.7 nm respectively are larger than the mean TEM

383 radius values of 3.9 and 13.9 nm respectively. It is evident that both techniques measure

384 significant coarsening at 700 °C.

385

386 *Precipitate size calculated from shape dependent model fitting*

387 In order to refine the real-space precipitate size estimates obtained from the SANS data,

388 model fitting was undertaken using the SasView software program [71]. This analysis

389 employed two different precipitate shape models namely a disk shape (radius, R_c, and

390 thickness, T_c, as given in equation 8) and an ellipsoid of revolution (polar axis, b, and

391 equatorial axis, a, as given in equation 9). An ellipsoid of revolution is also referred to as an

392 oblate spheroid and this term will be used hereafter. The disk model was considered in order

393 to be consistent with the Guinier analysis presented in the previous section whilst the oblate

394 spheroid shape was chosen as this shape has been one that has been assumed in previous

395 work on the IPP of VC studied by TEM e.g. in reference [19]. In both cases, the precipitates

396 were assumed to have a lognormal size dispersion of the major axis (i.e. R_c for the disk and

397 the equatorial axis, a, for the oblate spheroid). The magnitude of the dispersion was

398 expressed in terms of the dispersion parameter, σ, which is the standard deviation of the

399 lognormal distribution. The disk thickness and spheroid polar radius were assumed to have a

400 zero dispersion parameter.

401 The calculated 1-D nuclear scattering profiles were then fitted to the experimental 1-D

402 scattering curves using, as fixed parameters, the precipitate volume fractions, obtained from

403 equation 7, and the contrast between precipitates and ferrite matrix calculated from R(q)

404 (Table 2). The starting estimates in the model for the disk mean radius and half-thickness

405 (major and minor axes respectively in the case of the oblate spheroid) were the R and T

406 values found from the Guinier analysis. The goodness of fit between experimental and

407 calculated 1-D scattering profiles was determined using the well known chi-squared quantity

408 for all computations. The effect of altering the dispersion parameter in the range 0 to 0.5 was

409 explored and it was found that consistently better fitting was obtained with values of σ in the

410 range 0.1 to 0.3 than for larger values of σ. The Supplementary Data file provides a summary

411 of the calculations for both shapes and for different dispersion values.

412 As both the disk and oblate spheroid models give acceptable fitting results with very little

413 difference between them for all ageing times, we proceed by reporting the results (mean

414 equatorial radius of particles, a, and mean polar radius, b) given by the oblate spheroid model

415 for the mid-point polydispersity value, $\sigma=0.2$ (there was little difference in goodness of fit for

416 σ in the range 0.1 to 0.3) and refer the reader to the Supplementary Data file for the extended

417 calculations.

418 Figure 7 shows representative full model fitting plots using the oblate spheroid model with

419 $\sigma=0.2$. There is clearly good agreement over the full q-range for all the transformation times.

420 The mean values of particle dimensions obtained from the model calculations are listed in

421 Table 3 (where the dispersion parameter has been taken to be 0.2) along with the values of R

422 and T determined from the Guinier measurements of Figs. 6(c) and (d). It is evident that there

423 is generally reasonable agreement between R and a although some larger discrepancies do

424 arise in thickness values at the longest ageing time where the Guinier analysis gives

425 somewhat greater values.

426   The data listed in Table 3 for the Guinier measurements and the oblate spheroid model fitting

427   are plotted in Fig. 8 and the error bars on the model fitting data points correspond to

428   uncertainties generated from the calculations. Overall, there is seen to be good agreement

429   between particle radius and thickness from the Guinier method calculations and from the

430   model fitting.

431

432   **Further Discussion**

433   In this section we consider, first, the evidence from the SANS data regarding the composition

434   of the vanadium-containing precipitates and secondly the effect of the particle size and

435   volume fraction on the strengthening contribution of IPP to the ferrite phase.

436   **5.1 Effects of transformation time on composition of MX precipitates**

437   Information on the chemical composition of the precipitates (more generally written as MX

438   where M=V, Fe and X=C,N) can be gained from the ratio $R(q)$ of those samples in which the

439   γ has fully transformed to α and there is no residual martensite or bainite in the

440   microstructure following quenching, i.e. 300 and 600 min transformation times. The mean

441    $R(q)$ decreases from 1.09 to 0.98 (Table 2) suggesting a change in composition of the MX

442   phase. For stoichiometric VC, the value of R(q) from the contrast factors in Supplementary

443   Data is 1.23. The contrast factor for VN is larger than for VC so the substitution of N into the

444   MX phase in place of C cannot provide an explanation for the difference.

445   Thermodynamically it is feasible for Fe to substitute for V. Using Thermo-Calc and the

446   TCFE 7 database the full equilibrium calculation predicts 0.08 mol%Fe at 700 °C. However,

447   Fe substitution decreases the nuclear contrast factor, increases $R(q)$ and is not a consistent

448   explanation. An alternative to be considered is that the carbide phase is sub-stoichiometric

449   with respect to carbon. This would lead to a higher nuclear contrast factor and hence a

450   reduction in $R(q)$ in line with the experimental measurements.

451 Assuming a composition $VC_{0.90}$ gives a theoretical $R(q)$ of ~1.1 which is close to the

452 experimental value for the 300 min sample. This value is within the range of possible

453 compositions reported by Baker [2] and several researchers have measured a similar sub-

454 stoichiometry. For example, Oba et al. [60] found that in a medium carbon steel the value of x

455 ($x<1$) in VC_x is dependent on the transformation temperature whilst Zhang et al. [75] used

456 APT to shows that x is about 0.81 in Fe-0.1C-0.4V alloy isothermally transformed at 690 °C

457 for 48 hours. Furthermore, Ishiguro and Sato [76] used electron energy loss spectroscopy

458 (EELS) to identify non-stoichiometric MC_x in ultra-low carbon microalloy steels with x in the

459 range 0.82 to 0.91. Overall, a sub-stoichiometric vanadium carbide seems a possible

460 explanation for the present $R(q)$ measurements.

461 **5.2 Effect of transformation time on precipitate size and volume fraction**

462 The SANS data clearly demonstrate that changes in size and volume fraction (f_v) of IP

463 precipitates in a low carbon microalloy steel during isothermal ageing at 700°C can be

464 quantified.

465 There is a steady increase in f_v with transformation time which continues after the γ to α

466 transformation is complete (Table 2 and Fig. 9a) which suggests growth of the carbide from

467 supersaturated ferrite (α). Depending on the assumptions about the scattering length densities,

468 the volume percent after 600 min is in the range 0.22 to 0.28 vol%. This is consistent with the

469 equilibrium volume fraction of 0.30 vol% calculated using Thermo-Calc and the TCFE7

470 database.

471 In the present work, it is clear that precipitate dimensions, as represented by Guinier and

472 pseudo-Guinier radii both increase with ageing time at 700 °C. Real space particle

473 dimensions cannot be derived from the above model-independent parameters analytically for

474 polydisperse precipitate distributions [66, 69, 74]. However, from model fitting both an

475 oblate spheroid and disc model are found to give good fits to the data and to be in very

476 reasonable agreement with disc radius and thickness from the Guinier analysis. In Fig. 8,

477 dimensions from Guinier analysis are compared with the oblate spheroid dimensions from

478 model fitting. When the SANS results are compared with the somewhat limited TEM values,

479 the observations of an increase in radius with ageing time agree, as seen in Fig. 8(a) but the

480 TEM values are seen to be consistently smaller than those obtained from SANS. However, it

481 is not surprising that there is a discrepancy since the SANS measurements include orders of

482 magnitude more measurements than the TEM and the SANS measurements will include

483 random and grain boundary precipitates as well as the characteristic aligned rows and sheets

484 of interphase precipitation. Therefore, SANS will tend to measure a larger precipitate size

485 than the TEM method and the latter may well be biased to the IP precipitates with a row and

486 sheet morphology.

487 The measured increase in precipitate radius and thickness with ageing time is consistent with

488 the increasing volume fraction that is measured and is attributed to carbide growth from

489 supersaturated ferrite. To examine whether precipitates also undergo Ostwald ripening

490 (coarsening) the number density, N_v, was calculated based on the mean precipitate volume at

491 each transformation time and the variation of N_v with time is also shown on Fig. 9a.

492 Coarsening (decreasing N_v) is significant when ageing times exceed 60 min (3600 s) which

493 correlates approximately with the completion of the γ to α transformation (i.e. the cessation

494 of nucleation of new carbides by interphase precipitation). N_v is insensitive to whether disc or

495 oblate ellipsoid shapes are considered.

496 Comparison of the present number density data with values reported by Zhang, Kamikawa

497 and co-workers [15, 38, 75] on V-containing microalloy steels is not straightforward due to

498 differences in alloy composition and transformation temperatures and the fact that either

499 TEM or 3DAP were used to arrive at number density values. Zhang et al. [75] used 3DAP

500 and found mean number densities of the order of 5×10^{22} m^{-3} for a 0.2wt%V steel transformed

501 for 1 min at 690 °C. Zhang et al. [75] also shows that the number densities of VC increases

502 approximately 14 times when increase the V content from 0.2 wt% to 0.43 wt%. Kamikawa

503 et al. [38] used TEM and measured interparticle spacing in the range of 44 nm to 78 nm in

504 0.288 wt%V steels which had been transformed at 690 °C for 5 mins to 300 min at 690 °C.

505 This leads to number densities of 1.2×10^{22} m^{-3} to 2.1×10^{21} m^{-3} which (scaled to the present V

506 content of 0.2wt% according to Zhang et. al.'s study [75]) are from 2.2×10^{21} m^{-3} to 4×10^{20}

507 m^{-3} which agree well with the current SANS studies (Fig. 9a).

508

509 **5.3 Precipitation strengthening**

510 The strengthening mechanism of IP precipitates and their contribution to the strengthening of

511 ferrite was initially studied by Batte and Honecombe [11]. Subsequent work has shown that

512 the strengthening contribution depends on sheet spacing, particle spacing and particle mean

513 radius [18]. Recently, Kamikawa et al. [14] indicated that the Ashby-Orowan model gave a

514 better fit to IP precipitation strengthening than the Orowan equation [77] and we will apply

515 the former (eqn. 11 below) to the present data

$$516 \qquad \Delta\sigma_{ppt} = \frac{0.538 G b f_v^{0.5}}{2R} ln\left(\frac{R}{b}\right) \qquad (11)$$

517 $\Delta\sigma_{ppt}$ is the increase in yield strength, G is the shear modulus, b is the Burgers vector, f_v is the

518 carbide volume fraction and R is the mean carbide radius.

519 The values of $\Delta\sigma_{ppt}$ for the various ageing times are plotted alongside the microhardness data

520 in Fig. 9b and are seen to follow the same trend except at very short times. Microhardness

521 measurements reveal little difference in hardness between the samples aged for 3 and 5 min.

522 The sample aged for 60 min has a hardness which is slightly above those aged for 3 and

523 5 min but there is a clear and significant decrease in hardness for the longer holding times,

524 suggesting a marked reduction in the resistance to dislocation movement. The decreasing

525 yield strength increment beyond 60 min (3600 s) which is calculated from equation (11)

526 demonstrates that the decrease in ferrite hardness after 60 min is directly influenced by the

527 increasing particle radius which outweighs the increasing volume fraction of carbide

528 precipitate. In a recent study, Chen et al. [18] measured the IP contribution to ferrite

529 strengthening (in an alloy with 50% more V than in the present material) as 170 to 220 MPa

530 for somewhat lower transformation temperatures. This suggests the values from the simple

531 Ashby-Orowan equation used here are on the low side and that an improved model would

532 require direct microstructural data on sheet spacing and particle spacing that is not available

533 from SANS.

5. Conclusions

535 Small angle neutron scattering (SANS) was employed to quantify interphase precipitation in

536 samples of a V-containing, low-C microalloy steel which were isothermally transformed at

537 700 °C for various times followed by water quenching. It is shown to be important to extract

538 both nuclear and magnetic scattering signals so that nanoscale microally carbide precipitates

539 in partially transformed samples can be quantified. Results have been correlated with a

540 microstructural investigation using scanning electron and transmission electron microscopy

541 (TEM).

542   1. TEM observations confirmed the presence of fine-scale carbide precipitates, rich in V,

543   which exhibited the well-known interphase precipitate morphology of aligned rows

544   and sheets. Precipitates appeared to be either disc or oblate ellipsoid shaped with the

545   mean radius of the major axis increasing from ~4 to ~14 nm as the ageing time

546   increased from 5 to 600 min.

547   2. Analysis of the nuclear SANS data clearly reveals the presence of the nanoscale

548   precipitates in the isothermally transformed and quenched samples. From Kratky plots,

549   it is clear that the precipitate size and volume percent both increase with

550   transformation time. The latter increased from around 0.09 vol% to a value in the

551   range 0.22 to 0.28 vol% with ageing time.

3. Using simple model-independent Guinier analysis of the 1-D nuclear SANS plots, particle radii (R) and thickness values (T) were calculated. The radii increase with transformation time from ~ 10 to ~ 22 nm. The Guinier analysis was also used to show that the disc shaped precipitates have an aspect ratio of ~3. These values agree well with a model fitting analysis based on an oblate spheroid shape which showed an increased in the radius of the major axis from 9 to 18 nm. The precipitate number density decreases from 2×10^{21} to 5×10^{20} m^{-3} with increasing transformation time when an oblate ellipsoid model is employed for precipitate morphology.

4. The microhardness values of ferrite grains were measured and found to decrease from 215 to 150 Hv as the transformation time increased. They correlate well with the yield strength increments in the range 120 to 90 MPa calculated for different transformation times by using the mean carbide radius in the Ashby-Orowan model.

References

[1] F.B. Pickering, Physical Metallurgy and the Design of Steels, Applied Science Publishers, London, 1978.

[2] T.N. Baker, Processes, microstructure and properties of vanadium microalloyed steels, Materials Science and Technology 25(9) (2009) 1083-1107.

[3] T.N. Baker, Microalloyed steels, Ironmaking & Steelmaking 43(4) (2016) 264-307.

[4] J.R. Paules, Developments in HSLA steel products, JOM Journal of the Minerals, Metals and Materials Society 43(1) (1991) 41-44.

[5] G. Platts, A. Vassiliou, F. Pickering, Developments in microalloyed high-strength low-alloy steels: an overview, Metallurgist and materials technologist 16(9) (1984) 447-454.

[6] H. Stuart, The properties and processing of microalloyed HSLA steels, JOM Journal of the Minerals, Metals and Materials Society 43(1) (1991) 35-40.

[7] C.M. Sonsino, Light-weight design chances using high-strength steels, Materialwissenschaft und Werkstofftechnik 38(1) (2007) 9-22.

[8] D. Bhattacharya, Microalloyed steels for the automotive industry, Tecnologia em Metalurgia, Materiais e Mineraçao 11(4) (2014) 371.

[9] A. Kumar, S. Singh, K. Ray, Influence of bainite/martensite-content on the tensile properties of low carbon dual-phase steels, Materials Science and Engineering: A 474(1) (2008) 270-282.

[10] Y. Funakawa, T. Shiozaki, K. Tomita, T. Yamamoto, E. Maeda, Development of high strength hot-rolled sheet steel consisting of ferrite and nanometer-sized carbides, ISIJ international 44(11) (2004) 1945-1951.

[11] A. Batte, R. Honeycombe, Strengthening of ferrite by vanadium carbide precipitation, Metal Science 7(1) (1973) 160-168.

[12] A. Davenport, F. Berry, R. Honeycombe, Interphase precipitation in iron alloys, Metal Science 2(1) (1968) 104-106.

[13] D.P. Dunne, Review: Interaction of precipitation with recrystallisation and phase transformation in low alloy steels, Materials Science and Technology 26(4) (2010) 410-420.

[14] N. Kamikawa, Y. Abe, G. Miyamoto, Y. Funakawa, T. Furuhara, Tensile Behavior of Ti, Mo-added Low Carbon Steels with Interphase Precipitation, ISIJ international 54(1) (2014) 212-221.

[15] Y.-J. Zhang, G. Miyamoto, K. Shinbo, T. Furuhara, T. Ohmura, T. Suzuki, K. Tsuzaki, Effects of transformation temperature on VC interphase precipitation and resultant hardness in low-carbon steels, Acta Materialia 84 (2015) 375-384.

[16] C. Chen, H. Yen, F. Kao, W. Li, C. Huang, J. Yang, S. Wang, Precipitation hardening of high-strength low-alloy steels by nanometer-sized carbides, Materials Science and Engineering: A 499(1) (2009) 162-166.

[17] C.-Y. Chen, J.-R. Yang, C.-C. Chen, S.-F. Chen, Microstructural characterization and strengthening behavior of nanometer sized carbides in Ti–Mo microalloyed steels during continuous cooling process, Materials Characterization 114 (2016) 18-29.

[18] M.-Y. Chen, M. Gouné, M. Verdier, Y. Bréchet, J.-R. Yang, Interphase precipitation in vanadium-alloyed steels: Strengthening contribution and morphological variability with austenite to ferrite transformation, Acta Materialia 64 (2014) 78-92.

[19] G. Miyamoto, R. Hori, B. Poorganji, T. Furuhara, Interphase precipitation of VC and resultant hardening in V-added medium carbon steels, ISIJ international 51(10) (2011) 1733-1739.

[20] R. Lagneborg, T. Siwecki, S. Zajac, B. Hutchinson, The role of vanadium in microalloyed steels, Scand. J. Metall 28(5) (1999) 186-241.

[21] Y. Funakawa, K. Seto, Coarsening behavior of nanometer-sized carbides in hot-rolled high strength sheet steel, Materials science forum, Trans Tech Publ, 2007, pp. 4813-4818.

622   [22] J. Jang, Y. Heo, C. Lee, H. Bhadeshia, D.-W. Suh, Interphase precipitation in Ti-Nb and
623   Ti-Nb-Mo bearing steel, Materials Science and Technology 29(3) (2013) 309-313.
624   [23] J.H. Jang, C.-H. Lee, Y.-U. Heo, D.-W. Suh, Stability of (Ti, M) C (M= Nb, V, Mo and
625   W) carbide in steels using first-principles calculations, Acta Materialia 60(1) (2012) 208-217.
626   [24] W. Lee, S. Hong, C. Park, K. Kim, S. Park, Influence of Mo on precipitation hardening
627   in hot rolled HSLA steels containing Nb, Scripta Materialia 43(4) (2000) 319-324.
628   [25] W. Zemin, Z. Xiaoyong, L. wenqing, Influence of Mo on tempering precipitation in Nb-
629   Mo-V microalloyed steels, Chinese Journal of Materials research 24(2) (2010) 217-224.
630   [26] A. Davenport, R. Honeycombe, Precipitation of Carbides at $\ gamma $-$\ alpha
631    $ Boundaries in Alloy Steels, Proceedings of the Royal Society of London A: Mathematical,
632   Physical and Engineering Sciences, The Royal Society, 1971, pp. 191-205.
633   [27] J. Kim, J.-G. Jung, D.-H. Kim, Y.-K. Lee, The kinetics of Nb (C, N) precipitation during
634   the isothermal austenite to ferrite transformation in a low-carbon Nb-microalloyed steel, Acta
635   Materialia 61(19) (2013) 7437-7443.
636   [28] F. Bu, X. Wang, L. Chen, S. Yang, C. Shang, R. Misra, Influence of cooling rate on the
637   precipitation behavior in Ti–Nb–Mo microalloyed steels during continuous cooling and
638   relationship to strength, Materials Characterization 102 (2015) 146-155.
639   [29] H.J. Jun, K. Kang, C. Park, Effects of cooling rate and isothermal holding on the
640   precipitation behavior during continuous casting of Nb–Ti bearing HSLA steels, Scripta
641   Materialia 49(11) (2003) 1081-1086.
642   [30] S. Clark, V. Janik, A. Rijkenberg, S. Sridhar, Analysis of the extent of interphase
643   precipitation in V-HSLA steels through in-situ characterization of the γ/α transformation,
644   Materials Characterization 115 (2016) 83-89.
645   [31] N. Law, S. Parsons, P. Howell, D. Edmonds, Crystallography of carbide precipitation at
646   transformation interfaces during austenite decomposition in a low-alloy steel, Materials
647   science and technology 3(8) (1987) 642-648.
648   [32] R. Okamoto, A. Borgenstam, J. Ågren, Interphase precipitation in niobium-microalloyed
649   steels, Acta Materialia 58(14) (2010) 4783-4790.
650   [33] H.-W. Yen, P.-Y. Chen, C.-Y. Huang, J.-R. Yang, Interphase precipitation of nanometer-
651   sized carbides in a titanium–molybdenum-bearing low-carbon steel, Acta Materialia 59(16)
652   (2011) 6264-6274.
653   [34] G. Miyamoto, R. Hori, B. Poorganji, T. Furuhara, Crystallographic analysis of
654   proeutectoid ferrite/austenite interface and interphase precipitation of vanadium carbide in
655   medium-carbon steel, Metallurgical and Materials Transactions A 44(8) (2013) 3436-3443.
656   [35] Y.-J. Zhang, G. Miyamoto, K. Shinbo, T. Furuhara, Effects of α/γ orientation
657   relationship on VC interphase precipitation in low-carbon steels, Scripta Materialia 69(1)
658   (2013) 17-20.
659   [36] C. Chih-Yuan, C. Shih-Fan, C. Chien-Chon, Y. Jer-Ren, Control of precipitation
660   morphology in the novel HSLA steel, Materials Science and Engineering: A 634 (2015) 123-
661   133.
662   [37] T. Dorin, K. Wood, A. Taylor, P. Hodgson, N. Stanford, Effect of coiling treatment on
663   microstructural development and precipitate strengthening of a strip cast steel, Acta
664   Materialia 115 (2016) 167-177.
665   [38] N. Kamikawa, K. Sato, G. Miyamoto, M. Murayama, N. Sekido, K. Tsuzaki, T.
666   Furuhara, Stress–strain behavior of ferrite and bainite with nano-precipitation in low carbon
667   steels, Acta Materialia 83 (2015) 383-396.
668   [39] S. Mukherjee, I. Timokhina, C. Zhu, S. Ringer, P. Hodgson, Three-dimensional atom
669   probe microscopy study of interphase precipitation and nanoclusters in thermomechanically
670   treated titanium–molybdenum steels, Acta materialia 61(7) (2013) 2521-2530.

[40] S. Mukherjee, I. Timokhina, C. Zhu, S.P. Ringer, P.D. Hodgson, Clustering and precipitation processes in a ferritic titanium-molybdenum microalloyed steel, Journal of Alloys and Compounds 690 (2017) 621-632.

[41] R. Honeycombe, R. Mehl, Transformation from austenite in alloy steels, Metallurgical Transactions A 7(7) (1976) 915-936.

[42] H. Bhadeshia, Diffusional transformations: A theory for the formation of superledges, physica status solidi (a) 69(2) (1982) 745-750.

[43] P. Rios, Morphology of interphase precipitation in microalloyed steels, Journal of materials science letters 10(16) (1991) 981-983.

[44] W. Liu, Computer simulation of VC, Metallurgical Transactions A 24(10) (1993) 2195-2207.

[45] P. Rios, A model for interphase precipitation in stoichiometrically balanced vanadium steels, Journal of materials science 30(7) (1995) 1872-1878.

[46] R. Lagneborg, S. Zajac, A model for interphase precipitation in V-microalloyed structural steels, Metallurgical and Materials Transactions A 32(1) (2001) 39-50.

[47] M. Ohnuma, J. Suzuki, S. Ohtsuka, S.-W. Kim, T. Kaito, M. Inoue, H. Kitazawa, A new method for the quantitative analysis of the scale and composition of nanosized oxide in 9Cr-ODS steel, Acta materialia 57(18) (2009) 5571-5581.

[48] Toshio Murakami, Hitoshi Hatano, Goro Miyamoto, T. Furuhara, Effects of Ferrite Growth Rate on Interphase Boundary Precipitation in V Microalloyed Steels, ISIJ International 52(4) (2012) 616-625.

[49] M.-Y. Chen, M. Gouné, M. Militzer, Y. Bréchet, J.-R. Yang, Superledge Model for Interphase Precipitation During Austenite-to-Ferrite Transformation, Metallurgical and Materials Transactions A 45(12) (2014) 5351-5361.

[50] T. Dorin, A. Taylor, K. Wood, J. Wang, P. Hodgson, N. Stanford, Complex precipitation phenomena in strip cast steels with high sulfur and copper contents, Journal of Applied Crystallography 49(5) (2016) 1777-1785.

[51] T. Dorin, K. Wood, A. Taylor, P. Hodgson, N. Stanford, Quantitative examination of carbide and sulphide precipitates in chemically complex steels processed by direct strip casting, Materials Characterization 112 (2016) 259-268.

[52] P. Staron, B. Jamnig, H. Leitner, R. Ebner, H. Clemens, Small-angle neutron scattering analysis of the precipitation behaviour in a maraging steel, Journal of applied crystallography 36(3) (2003) 415-419.

[53] G. Albertini, F. Carsughi, R. Coppola, F. Fiori, F. Rustichelli, M. Stefanon, Small-angle neutron scattering microstructural investigation of MANET steel, Journal of nuclear materials 233 (1996) 253-257.

[54] B.S. Seong, E. Shin, S.-H. Choi, Y. Choi, Y.S. Han, K.H. Lee, Y. Tomota, Quantitative analysis of fine nano-sized precipitates in low-carbon steels by small angle neutron scattering, Applied Physics A 99(3) (2010) 613-620.

[55] F. Perrard, A. Deschamps, F. Bley, P. Donnadieu, P. Maugis, A small-angle neutron scattering study of fine-scale NbC precipitation kinetics in the α-Fe–Nb–C system, Journal of applied crystallography 39(4) (2006) 473-482.

[56] H. Yasuhara, K. Sato, Y. Toji, M. Ohnuma, J.-i. Suzuki, Y. Tomota, Size analysis of nanometer titanium carbide in steel by using small-angle neutron scattering, Tetsu To Hagane 96(9) (2010) 545-549.

[57] A. Deschamps, F. Danoix, F. De Geuser, T. Epicier, H. Leitner, M. Perez, Low temperature precipitation kinetics of niobium nitride platelets in Fe, Materials Letters 65(14) (2011) 2265-2268.

[58] J. Wiskel, D. Ivey, H. Henein, The effects of finish rolling temperature and cooling interrupt conditions on precipitation in microalloyed steels using small angle neutron scattering, Metallurgical and Materials Transactions B 39(1) (2008) 116-124.

[59] N. Van Dijk, W. Bouwman, S. Offerman, M.T. Rekveldt, J. Sietsma, S. Van der Zwaag, A. Bodin, R. Heenan, High temperature SANS experiments on Nb (C, N) and MnS precipitates in HSLA steel, Metallurgical and Materials Transactions A 33(7) (2002) 1883-1891.

[60] Y. Oba, S. Koppoju, M. Ohnuma, T. Murakami, H. Hatano, K. Sasakawa, A. Kitahara, J.-i. Suzuki, Quantitative Analysis of Precipitate in Vanadium-microalloyed Medium Carbon Steels Using Small-angle X-ray and Neutron Scattering Methods, ISIJ international 51(11) (2011) 1852-1858.

[61] J. Scott, F.T. Docherty, M. MacKenzie, W. Smith, B. Miller, C.L. Collins, A.J. Craven, Sample preparation for nanoanalytical electron microscopy using the FIB lift-out method and low energy ion milling, Journal of Physics: Conference Series 26(1) (2006) 223.

[62] C.A. Schneider, W.S. Rasband, K.W. Eliceiri, NIH Image to ImageJ: 25 years of image analysis, Nature methods 9(7) (2012) 671-675.

[63] R. Heenan, S. Rogers, D. Turner, A. Terry, J. Treadgold, S. King, Small angle neutron scattering using Sans2d, Neutron News 22(2) (2011) 19-21.

[64] W. Woo, V. Em, E. Shin, P. Mikula, V. Ryukhtin, Influence of multiple small-angle neutron scattering on diffraction peak broadening in ferritic steel, Journal of Applied Crystallography 48(2) (2015) 0-0.

[65] A. Michels, J. Weissmüller, Magnetic-field-dependent small-angle neutron scattering on random anisotropy ferromagnets, Reports on Progress in Physics 71(6) (2008) 066501.

[66] F. De Geuser, A. Deschamps, Precipitate characterisation in metallic systems by small-angle X-ray or neutron scattering, Comptes Rendus Physique 13(3) (2012) 246-256.

[67] G.T. Wignall, F. Bates, Absolute calibration of small-angle neutron scattering data, Journal of applied crystallography 20(1) (1987) 28-40.

[68] O. Glatter, O. Kratky, Small angle scattering, Academic, New York (1982).

[69] A. Deschamps, F. De Geuser, On the validity of simple precipitate size measurements by small-angle scattering in metallic systems, Journal of Applied Crystallography 44(2) (2011) 343-352.

[70] T. Imae, T. Kanaya, M. Furusaka, N. Torikai, Neutrons in soft matter, John Wiley & Sons2011.

[71] SasView, SasView for Small Angle Scattering Analysis. http://www.sasview.org/index.html, 2017 (accessed 4th January 2017.).

[72] N. Kamikawa, M. Hirohashi, Y. Sato, E. Chandiran, G. Miyamoto, T. Furuhara, Tensile Behavior of Ferrite-martensite Dual Phase Steels with Nano-precipitation of Vanadium Carbides, ISIJ International 55(8) (2015) 1781-1790.

[73] F. Cousin, Small angle neutron scattering, EPJ Web of Conferences, EDP Sciences, 2015, p. 01004.

[74] A. Deschamps, F. De Geuser, Quantitative characterization of precipitate microstructures in metallic alloys using small-angle scattering, Metallurgical and Materials Transactions A 44(1) (2013) 77-86.

[75] Y.-J. Zhang, G. Miyamoto, K. Shinbo, T. Furuhara, Quantitative measurements of phase equilibria at migrating α/γ interface and dispersion of VC interphase precipitates: Evaluation of driving force for interphase precipitation, Acta Materialia 128 (2017) 166-175.

[76] Y. Ishiguro, K. Sato, Determination of non-stoichiometric composition of complex carbon-nitrides in steel by measuring plasmon energy, Materials Transactions, JIM 37(4) (1996) 643-649.

[77] T. Gladman, Precipitation hardening in metals, Materials Science and Technology 15(1) (1999) 30-36.

771 Figure 1. Experimental configuration used in the current SANS measurements. (a) An
772 incident neutron beam transmitted through a specimen containing (b) nano-sized precipitates
773 embedded in a ferritic matrix. (c) The resultant SANS two-dimensional pattern in the
774 presence of a horizontal magnetic field. (d) One-dimensional plot of the 'nuclear+magnetic'
775 and nuclear scattering intensities.

776 Figure 2. SEM images of the samples isothermally transformed at 700°C for various times
777 and water quenched. (a) directly water quenched; (b) – (d) isothermally transformed for 3, 5
778 and 60 min respectively showing ferrite grains (F) and regions of bainite (B) (transformed γ).
779 (e) and (f) 300 and 600 min isothermal transformation times respectively. Coarsened
780 interphase precipitates visible in (f).

781 Figure 3, Bright field TEM images of periodic interphase precipitation taken from the
782 samples isothermally transformed at 700°C for (a) 5 min and (b) 600 min. (c-d) High
783 resolution TEM lattice image from the sample held for 600 min, (d) elucidating the disc
784 nature of the precipitates and (e) EDX map for V.

785 Figure 4. One-dimensional SANS patterns of intensity versus scattering vector obtained from
786 the following samples: (a) water-quenched and (b) to (d) isothermally transformed.
787 Transformation times of: (b) 3 min, (c) 60 min, (d) 300 min. In (a)-(c) there is a clear
788 difference between nuclear and magnetic signals. In (d) they are virtually identical. Line of
789 slope -4 is shown for reference on the log-log plot.

790 Figure 5. Plot of $R(q)$ versus scattering vector calculated from the scattering curves in Fig. 4
791 for the water-quenched alloy and for the samples isothermally transformed for the times
792 shown. $R(q)$ is the ratio of magnetic to nuclear scattering intensity (equation 3). The
793 theoretical value for VC is shown by the horizontal line.

794 Figure 6. SANS nuclear scattering data from the samples isothermally transformed at 700 °C
795 following subtraction of Porod Law behaviour and incoherent scattering background.
796 Transformation times shown by the symbols on the plots. (a) Plots of I versus q; (b) the
797 corresponding Iq^2 versus q Kratky plots; (c) the first Guinier plot of ln(I) versus q^2; (d) the
798 second Guinier plot of ln(q^2I) $versus$ q^2.

799 Figure 7. Experimental SANS nuclear scattering data plotted as I $versus$ q from samples
800 transformed for the times shown (symbols) along with model fitted data (solid lines) using an
801 oblate spheroid model with dispersion parameters of 0 and 0.2 for the polar and equatorial
802 radii respectively.

803 Figure 8. Graphs to show the effect of isothermal holding time, t on particle dimensions
804 obtained from Guinier analysis and model fitting. Data are shown for R (radius) and T
805 (thickness) calculated from Guinier plots and a and $2b$ from oblate spheroid model fitting. (a)
806 is a plot of R and a (oblate spheroid major axis) versus time; (b) is a plot of T and $2b$ ($b=$
807 oblate spheroid minor axis) versus time. TEM measurements are radii calculated from major
808 axis diameters.

809 .

810 Figure 9. (a) Effect of isothermal holding time, t, on precipitate number density (left hand
811 axis) and volume fraction (right hand axis) determined from SANS data. (b) Effect of
812 isothermal holding time, t, on measured microhardness, Hv, (left hand axis) and calculated
813 yield strength increment (right hand axis). Error bars in Hv correspond to one standard
814 deviation from the mean.

815

816   Table 1. Chemical composition of vanadium microalloyed steel in weight percent (wt%) and
817   atomic percent (at%).

818   Table 2. Characteristics of the VX precipitates determined from analysis of SANS data for
819   samples isothermally transformed at 700 °C for different times. R_{max}, R_g, R_{g1}, R_{g2}, and f_v are
820   defined in section 3. $R(q)$ is the ratio of magnetic to nuclear scattering intensity.
821
822   Table 3. Average precipitate dimensions determined from analysis of SANS data for samples
823   isothermally transformed for different times. R and T are the average radius and thickness of
824   precipitate discs determined from the Guinier measurements of R_{g1}, R_{g2}. a and b are average
825   equatorial and polar radii respectively from model fitting with an oblate spheroid. ($2b$ is polar
826   diameter for direct comparison with T). σ_a is the dispersion parameter of a in model fitting.

Table 1.

Chemical composition of vanadium microalloyed steel in weight percent (wt%) and atomic percent (at%).

	C	Mn	Si	Al	P	S	V	N (ppm)	Fe
wt%	0.047	1.60	0.18	0.043	0.013	0.005	0.20	50	Bal.
at%	0.22	1.62	0.36	0.009	0.023	0.009	0.22	200	Bal.

Table 2

Calculated precipitate characteristics determined from model-independent analysis of SANS data for samples isothermally transformed for different times. R_{g1}, R_{g2}, R_{max}, and f_v are defined in section 3. R(q) is the ratio of magnetic to nuclear scattering intensity.

Transformation time (min)	R_{g1} (nm)	R_{g2} (nm)	R_{max} (nm)	Mean R(q)	f_v (%) (mean R(q))	f_v (%) (constant $\Delta\rho_{nuc}$)
3	6.9	0.8	4.4	-	-	0.094
5	8.3	0.9	5.2	-	-	0.13
60	10.6	1.0	6.8	-	-	0.18
300	13.0	1.7	9.8	1.09	0.21	0.24
600	15.5	2.3	12.6	0.98	0.22	0.28

Table 3

Average precipitate dimensions determined from analysis of SANS data for samples isothermally transformed for different times. R and T are the average radius and thickness of precipitate discs determined from the Guinier measurements of R_{g1}, R_{g2}. a and b are average equatorial and polar radii respectively from model fitting with an oblate spheroid. ($2b$ is polar diameter for direct comparison with T). σ_a is the dispersion parameter of a in model fitting.

Transformation time (min)	Calculated from Guinier measurements		Oblate spheroid model fitting (σ_a =0.2)	
	R (nm)	T (nm)	a (nm)	2b (nm)
3	9.8	2.8	9.1	2.7
5	11.6	3.0	10.4	2.8
60	14.9	3.3	11.5	3.3
300	18.2	5.7	14.8	4.8
600	21.7	8.0	17.5	6.2
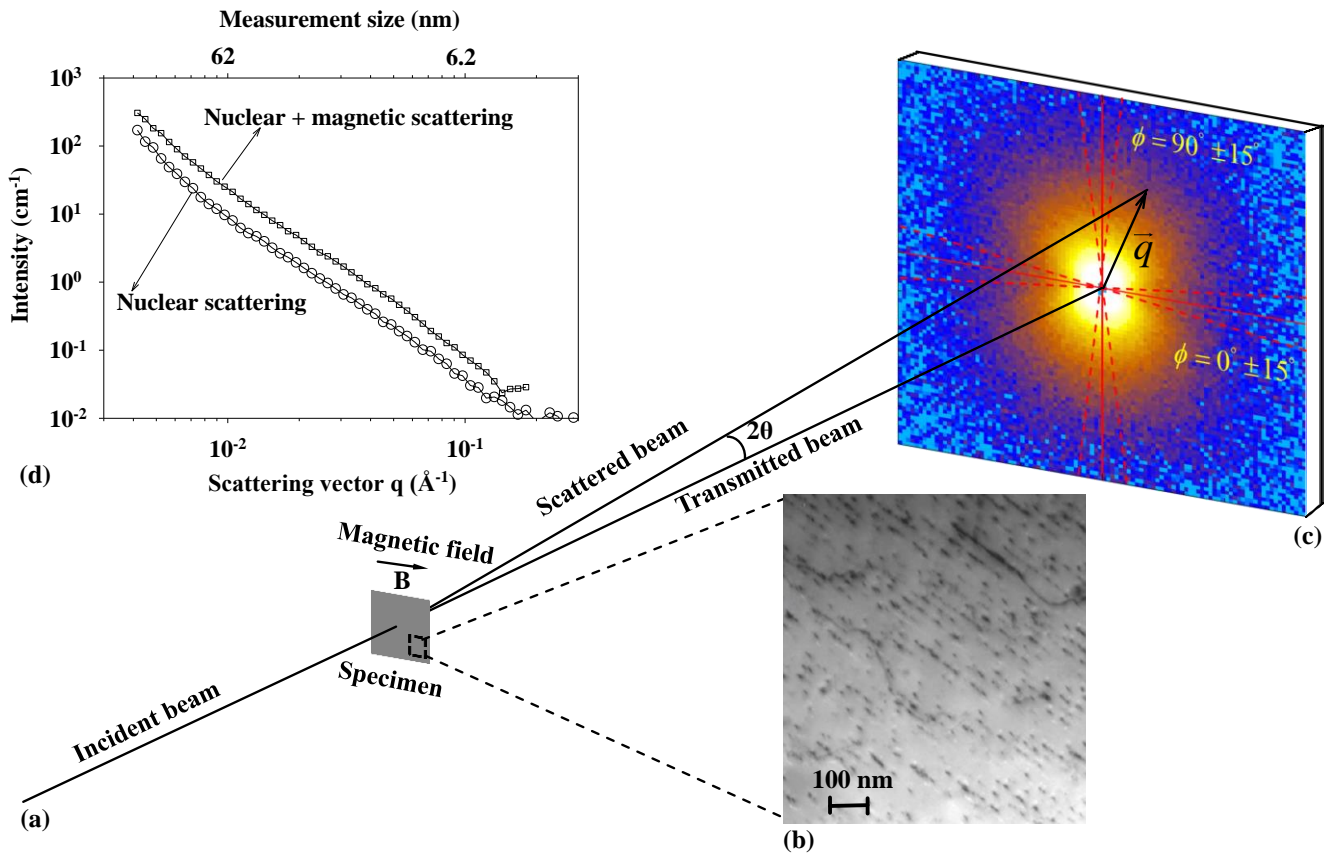
Figure 1. Experimental configuration used in the current SANS measurements. (a) An incident neutron beam transmitted through a specimen containing (b) nano-sized precipitates embedded in ferritic matrix. (c) The resultant SANS two-dimensional pattern in the presence of a horizontal magnetic field. (d) One-dimensional plot of the 'nuclear+magnetic' and nuclear scattering intensities.
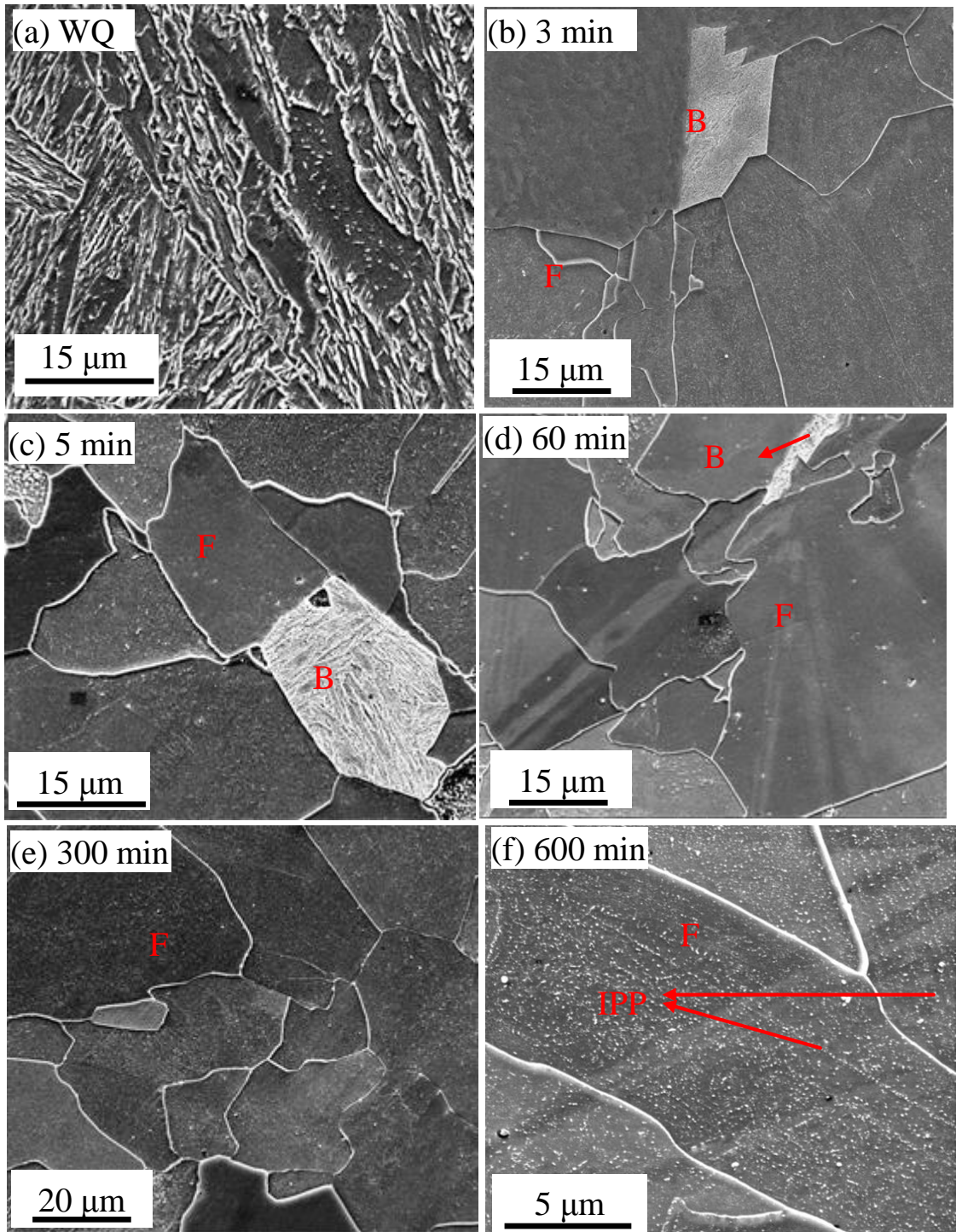
Figure 2. SEM images of the samples isothermally transformed at 700 °C for various times and water quenched. (a) directly water quenched; (b) – (d) isothermally transformed for 3, 5 and 60 min respectively showing ferrite grains (F) and regions of bainite (B) (transformed γ). (e) and (f) 300 and 600 min isothermal transformation times respectively. Coarsened interphase precipitates visible in (f).
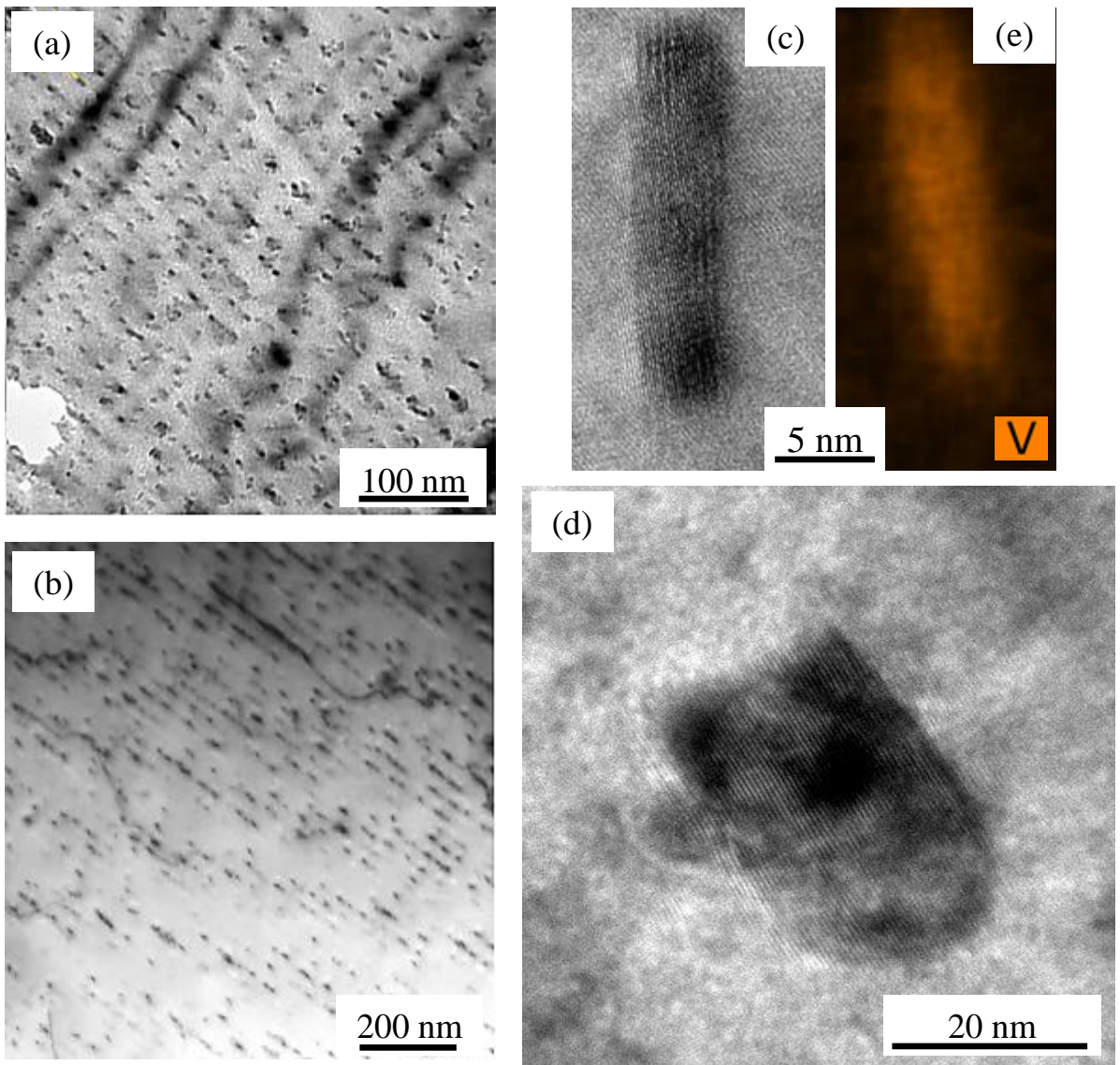
Figure 3. Bright field TEM images of periodic interphase precipitation taken from the samples isothermally transformed at 700°C for (a) 5 min and (b) 600 min. (c-d) High resolution TEM lattice image from the sample held for 600 min, (d) elucidating the disc nature of the precipitates and (e) EDX map for V.
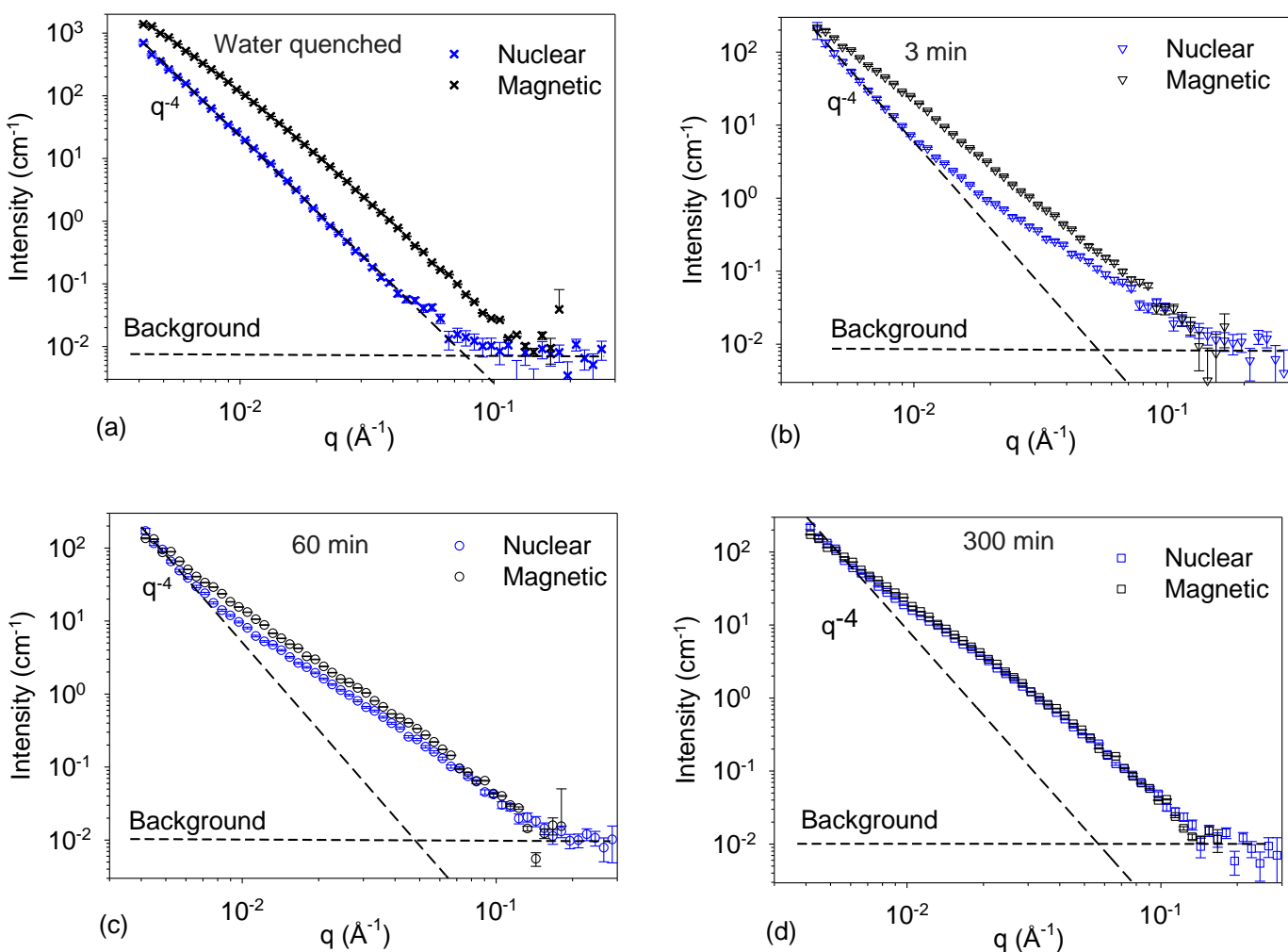
Figure 4. One-dimensional SANS patterns of intensity versus scattering vector obtained from the following samples: (a) water-quenched and (b) to (d) isothermally transformed. Transformation times for (b) 3 min, for (c) 60 min and for (d) 300 min. In (a), (b) and (c) there is a clear difference between nuclear and magnetic signals. In (d) they are virtually identical. Line of slope -4 is shown for reference on the log-log plot.
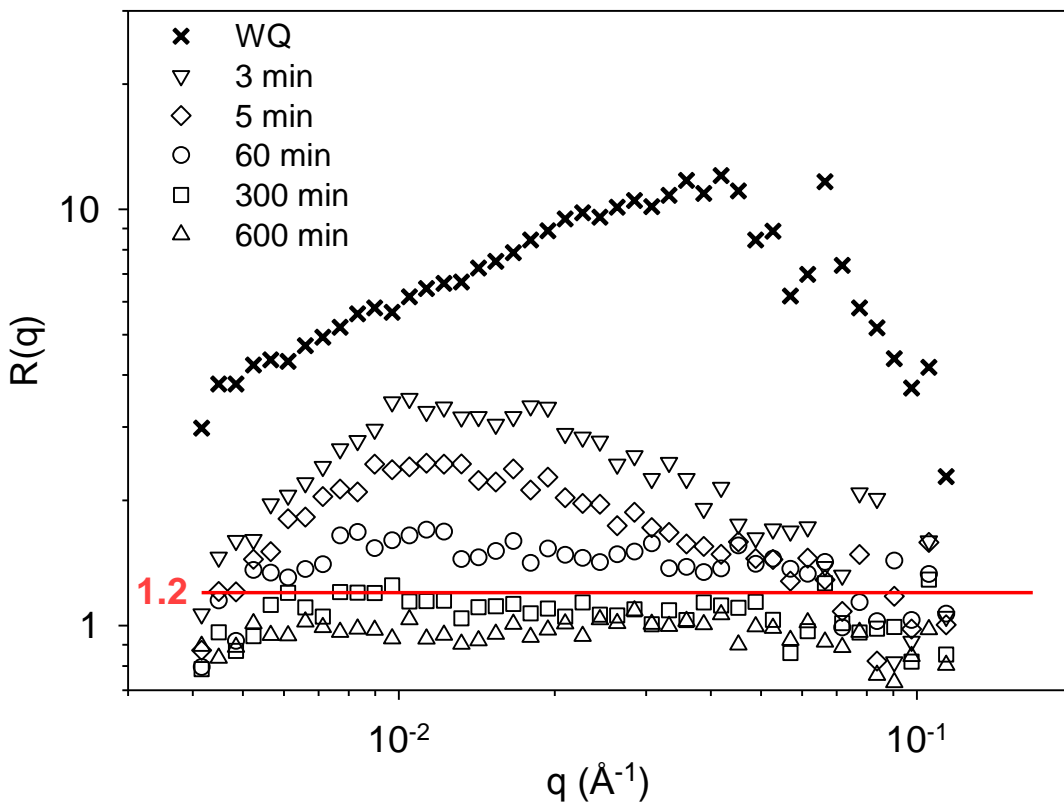
Figure 5. Plot of R(q) as a function of scattering vector calculated from the scattering curves in Fig. 5 for the water-quenched alloy and for samples isothermally transformed for the times shown. R(q) is the ratio of magnetic to nuclear scattering intensity(equation 3). The theoretical value for VC is shown by the horizontal line
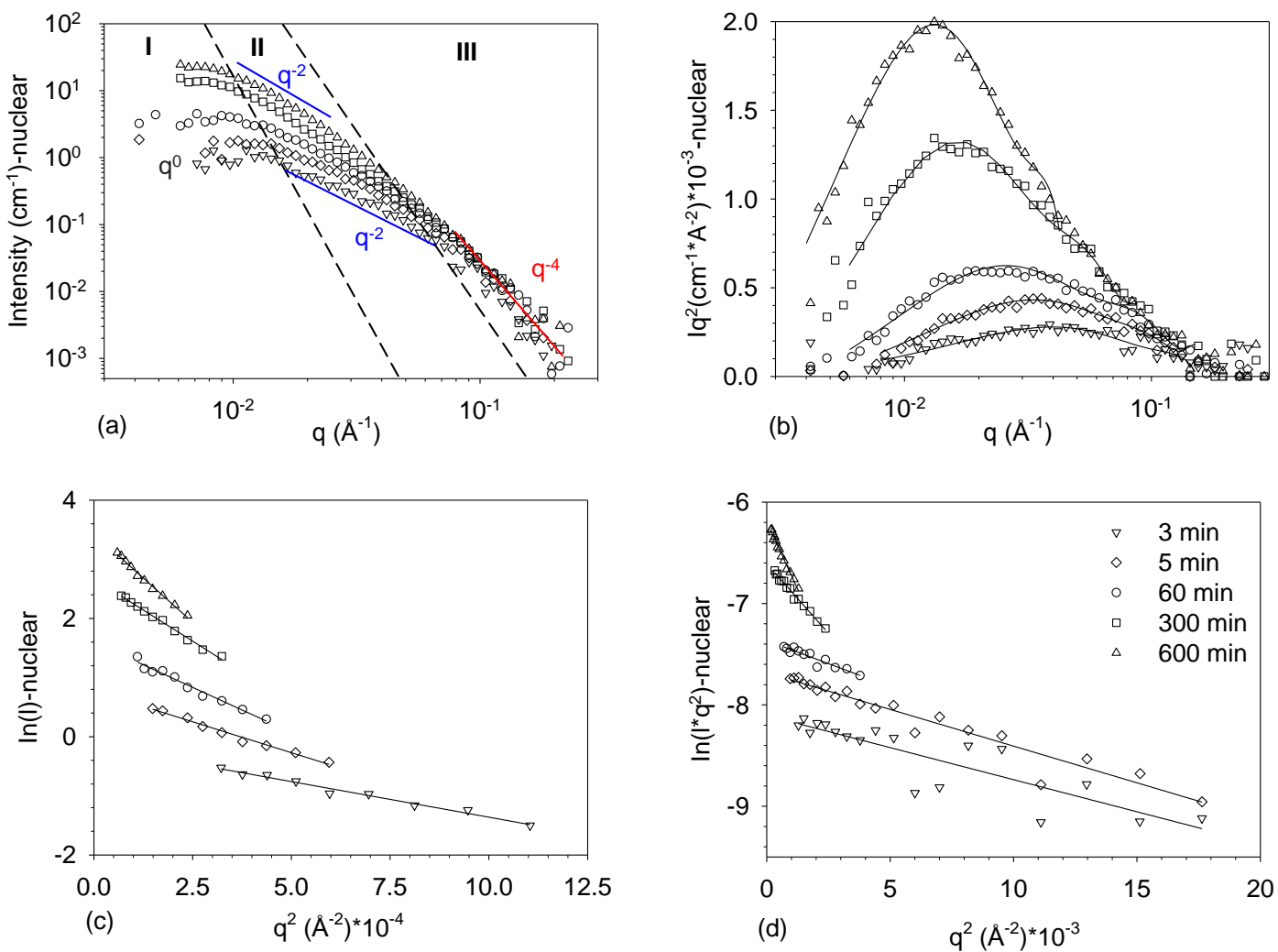
Figure 6. (a) SANS nuclear scattering data following subtraction of Porod behaviour and incoherent scattering background from the samples isothermally transformed at 700 °C for the times shown by the symbols; (b) the corresponding Iq^2 versus q Kratky plots (c) the first Guinier plot of $\ln(I)$ versus q^2 ; (d) the second Guinier plot of $\ln(q^2I)$ versus q^2.

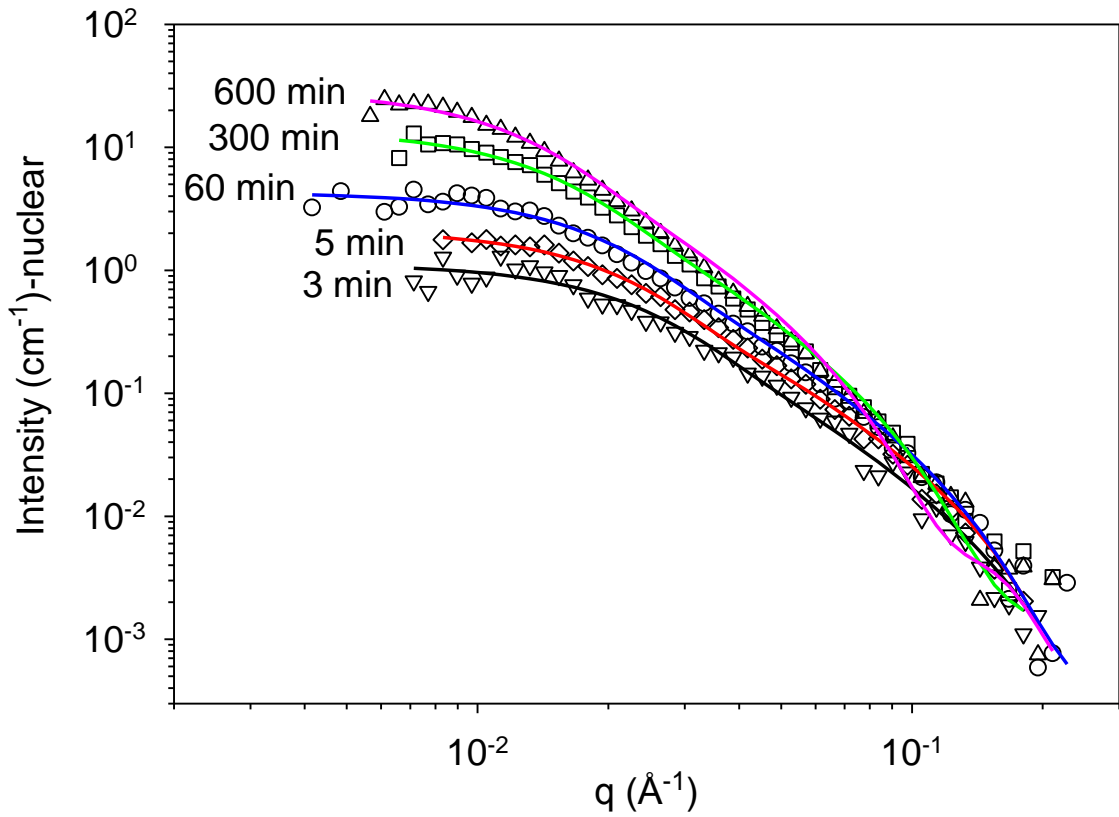Figure 7. Experimental SANS nuclear scattering data plotted as *I versus q* from samples transformed for the times shown (symbols) along with model fitted data (solid lines) using an oblate spheroid model with dispersion parameters of 0 and 0.2 for the polar and equatorial radii respectively.
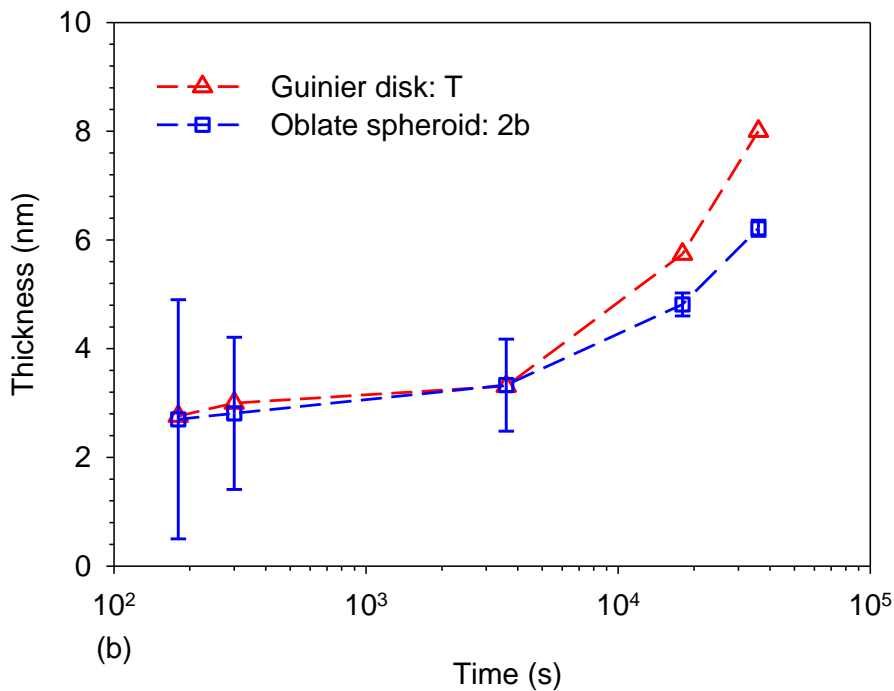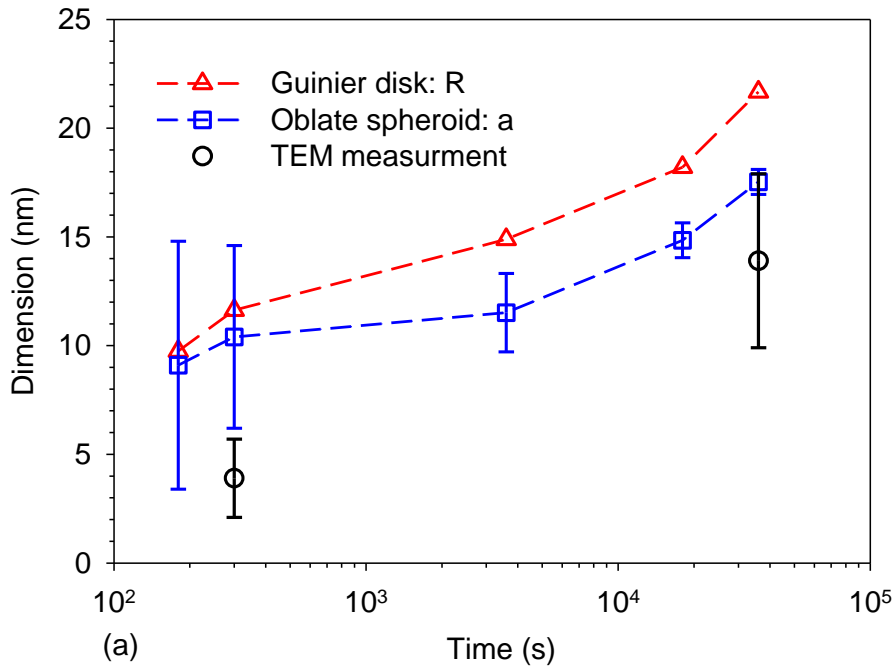
Figure 8. Graphs to show the effect of isothermal holding time, t on particle dimensions obtained from Guinier analysis and model fitting. Data are shown for R (radius) and T (thickness) calculated from Guinier plots and a and $2b$ from oblate spheroid model fitting. (a) is a plot of R and a (oblate spheroid major axis) versus time; (b) is a plot of T and $2b$ (b= oblate spheroid minor axis) versus time. TEM measurements are radii calculated from major axis diameters.
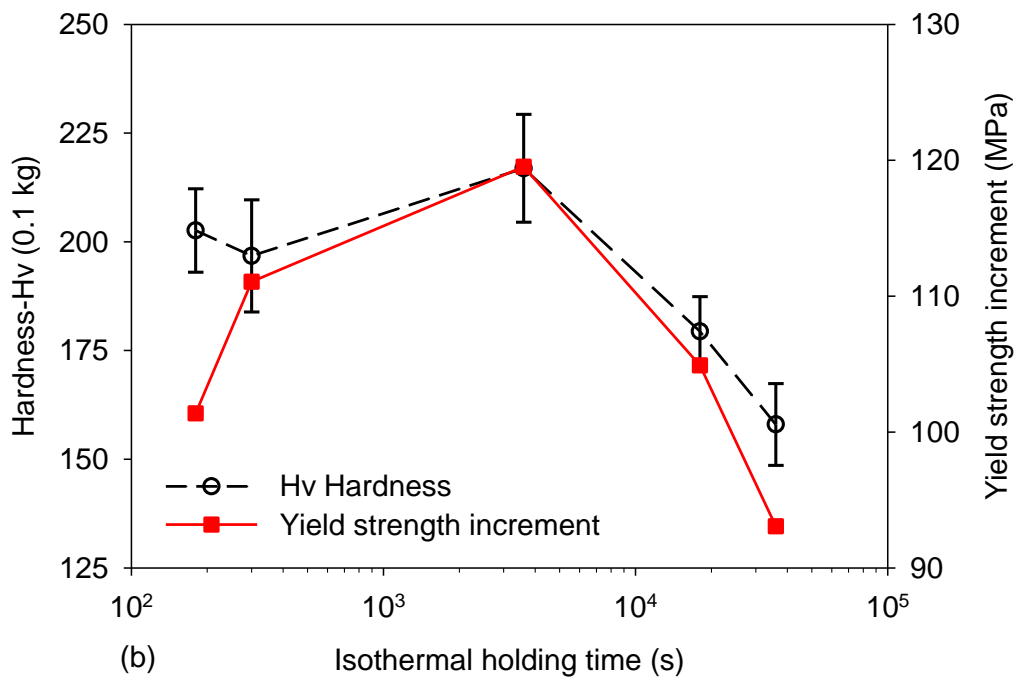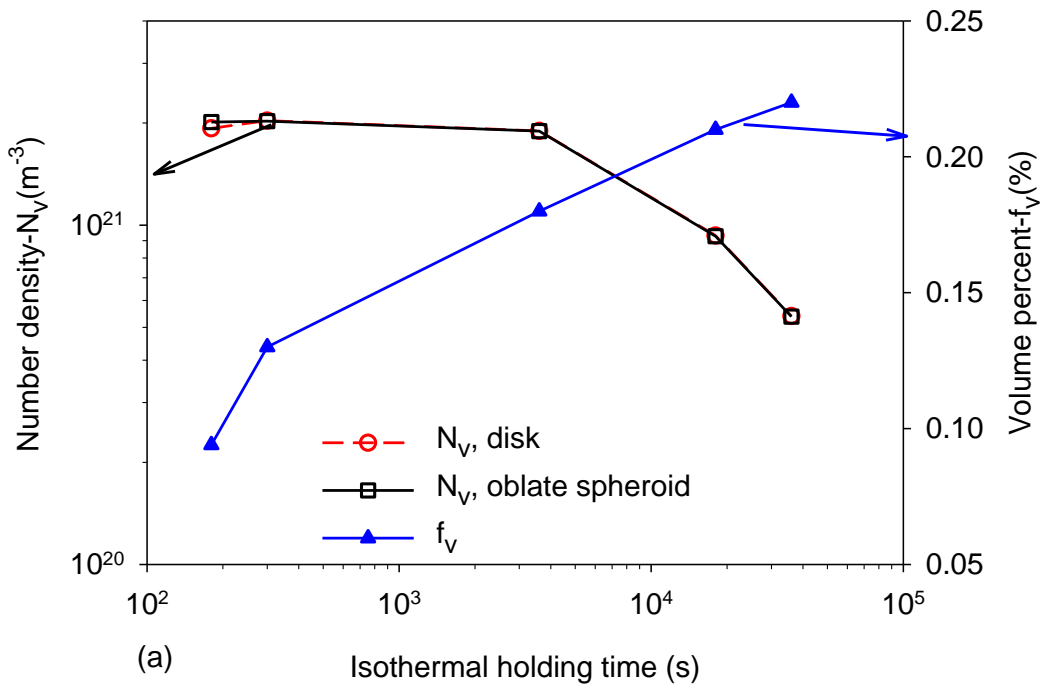
Figure 9. (a) Effect of isothermal holding time, t, on precipitate number density (left hand axis) and volume percent (right hand axis) determined from SANS data. (b) Effect of isothermal holding time, t, on measured microhardness, Hv, (left hand axis) and calculated yield strength increment (right hand axis). Error bars in Hv correspond to one standard deviation from the mean.

Supplementary

Supplementary Note 1 – Selection of austenitization and transformation temperatures

The austenitization temperature and time were selected to dissolve Fe_3C or vanadium carbonitride (VX) precipitates already present in the steel. Calculations performed using Thermo-Calc and the TCFe7 database indicate that in this steel VX becomes unstable above approximately 1050 °C. The isothermal treatment temperature of 700 °C was chosen to obtain a ferritic microstructure with nanoscale interphase VX precipitates and to allow precipitate growth and coarsening to occur at the more extended holding times.

Supplementary Note 2 – Methodology of small angle neutron scattering experiments

The specimens for SANS were sectioned from the heat treated materials using a precision saw and then mechanically polished using a 4 step standard metallographic preparation approach to 1.0 μm diamond finish prior to the SANS measurements. The specimen dimensions were approximately 10 mm × 10 mm × ~1 mm (thickness). The thicknesses at nine different positions on each specimen were accurately measured using micrometer and a mean value calculated. The neutron beam was 8 mm in diameter giving a scanned volume of approximately 50 mm^3 and containing over 10^5 grains. The data acquisition time was 60 minutes for each specimen. Scattered neutrons were recorded by two arrays of position sensitive area detectors each ~ 1 m^2, one located 2.38 m behind the sample and the other 4 m behind the sample. This configuration gives small angle scattering vector (*q*) values between 0.004 and 0.3 $Å^{-1}$, where $q= 4\pi sin\theta/\lambda$ and the scattering angle is 2θ. This corresponds very approximately to characteristic particle sizes, d, ranging from ~ 1.5 nm to 80 nm (assuming $d\sim2\pi/q$).

Supplementary Note 3 – Data used in SANS analysis

3.1. Magnetic scattering length densities

The magnetic scattering length density (SLD) of the ferrite matrix, ρ_{mag}^m is given by the equation

$$\rho_{mag}^m = \frac{\rho_0 u}{v}$$

where $\rho_0 = 2.7 \times 10^{-15}$ m is a constant, $u = 2.1869$ is the mean atomic magnetic moment of the matrix and $v = 11.7 \times 10^{-30}$ m^3 is the mean volume per atom [71]. The value obtained for ρ_{mag}^m is $5.04 \times 10^{14} m^{-2}$. In SANS, precipitate phases which are paramagnetic or diamagnetic are generally considered to have a zero magnetic SLD. This applies to common precipitates in steel such as Fe$_3$C and MX carbonitrides (where M =Ti, Mo, Nb, V and X=C, N). Thus the magnetic contrast factor $\Delta\rho_{mag}$ where $\Delta\rho_{mag} = \rho_{mag}^p - \rho_{mag}^m$ is taken to be $-5.04 \times 10^{14} m^{-2}$.

3.2. Nuclear scattering length densities

The nuclear scattering length density of a phase, i, is calculated from the equation

$$\rho_{nuc}^i = \frac{\sum x_i\, b_i}{v_i}$$

where x_i is the atom fraction of i in the phase, v_i is the atomic volume and b_i is the coherent nuclear scattering length density of element i [72]. The nuclear contrast factor is $\Delta\rho_{nuc}$ where $\Delta\rho_{nuc} = \rho_{nuc}^p - \rho_{nuc}^m$. Table A1 lists the nuclear SLD and nuclear contrast factor for i=matrix and i=precipitates relevant to the present study along with values of *R(q)*, the ratio of magnetic to nuclear scattering intensity

2

Table SN 3-1

Values of nuclear scattering length density, nuclear contrast factor and $R(q)$ phases potentially relevant to this study.

Phase	ρ_{nuc} $(10^{14}m^{-2})$	ρ_{mag} $(10^{14}m^{-2})$	$\Delta\rho_{nuc}$ $(10^{14}m^{-2})$	$\Delta\rho_{mag}$ $(10^{14}m^{-2})$	$R(q)=(\Delta\rho_{mag}/\Delta\rho_{nuc})^2$
Fe	7.93	5	0	0	-
Fe_3C	6.73	0	1.2	5	17.36
MnS	-0.249	0	8.179	5	0.37
VC	3.43	0	4.5	5	1.23
VN	5.07	0	2.86	5	3.05
TiN	3.04	0	4.89	5	1.04

It is clear that all potential precipitate phases will contribute strongly to the magnetic contrast but VC and any MnS that might form will dominate the nuclear contrast although the latter is likely to form micron size phase outside the range of detection of the SANS detectors. Fe_3C, on the other hand, has a relatively small contrast factor. It is also notable that VC has magnetic and nuclear contrast factors that are close, with a ratio ~ 1.2 whereas the ratio for V(C, N) is larger reaching ~ 3 for VN.
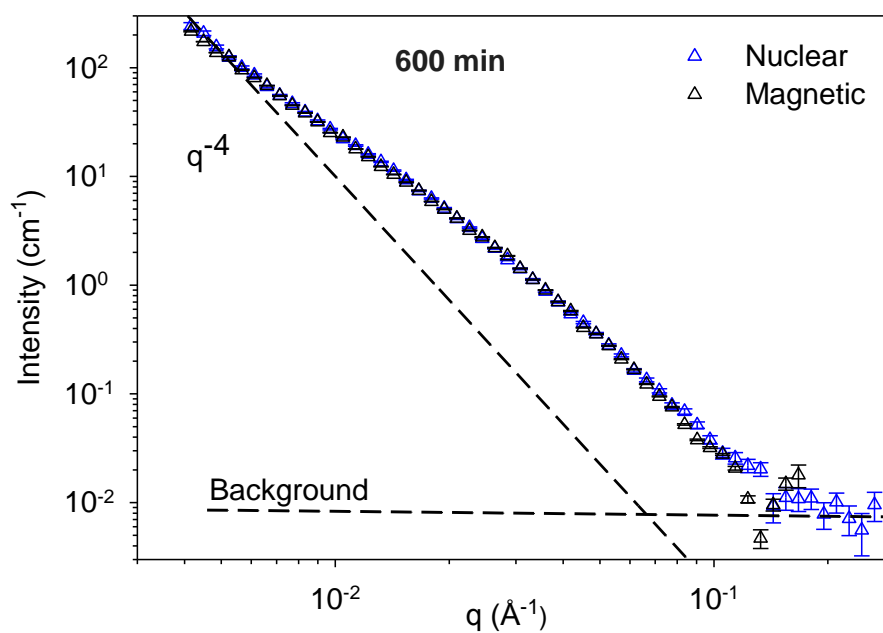
Supplementary Note 4 - One-dimensional SANS patterns from the alloy after isothermal transformation for 600 min.

Supplementary Note 5 – comparison of SasView model fitting for a disc shape and an oblate spheroid shape (also termed oblate ellipsoid of revolution)

The fitting procedure is described in the main text and compared a disc shaped model with an oblate spheroid model. The calculated 1-D nuclear scattering profiles were fitted to the experimental 1-D scattering curves using, as fixed parameters, the precipitate volume fractions, obtained from equation 7, and the contrast between precipitates and ferrite matrix calculated from R(q) (Table 2). Two different particle shapes were investigated namely a disc shape and an oblate spheroid shape. The starting estimates in the model for the disc mean radius (R) and half-thickness (T/2) (major, *a*, and minor, *b*, axes in the case of the oblate spheroid) were the radius and thickness values found from the Guinier model-independent analysis.

The goodness of fit between experimental and calculated 1-D scattering profiles was determined using the well known chi-squared quantity for all computations. The effect of altering the dispersion parameter in the range 0 to 0.6 for the major axis was explored; the polydispersity of the minor axis was set to zero as initial trials showed that varying this had a negligible effect on the fitting results. It was found that consistently better fitting was obtained with values of σ in the range 0.1 to 0.3 than for larger values of σ.

Representative graphs of experimental SANS nuclear scattering data plotted as *I versus q* from samples transformed for the time shown (symbols) along with model fitted data (solid lines) using either an oblate spheroid model or a disc model are shown in Figs. SN 5.1 (a) and (b) (3 min transformation) and SN 5.2 (a) and (b) (300 min transformation). It is clear from these figures that a polydispersity value (PD) of 0.2 fitted better than 0 or 0.5. However, there is very little difference in the fitting of oblate spheroid (frequently termed an oblate ellipsoid of revolution) or disc. Both appear to fit the experimental data well.
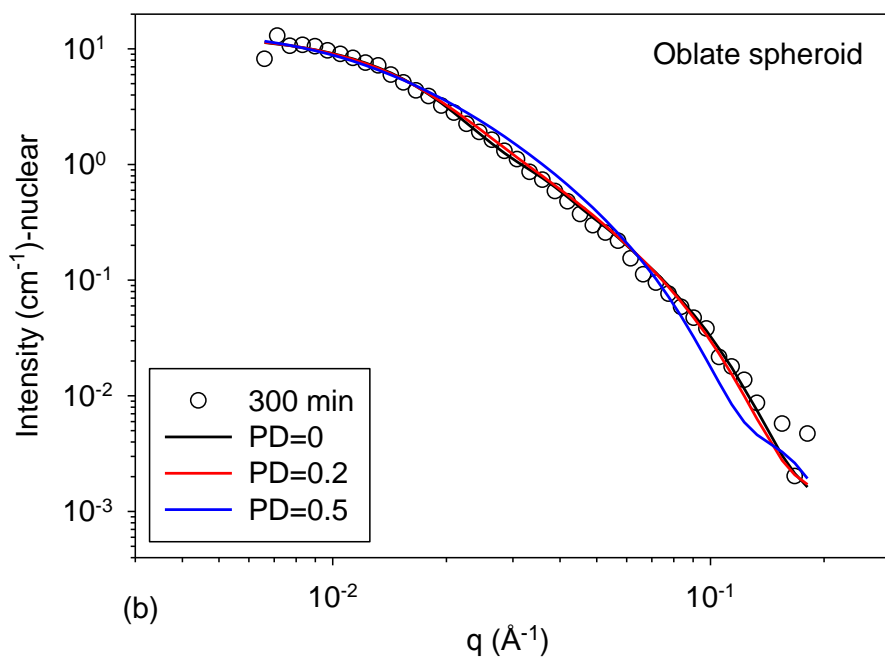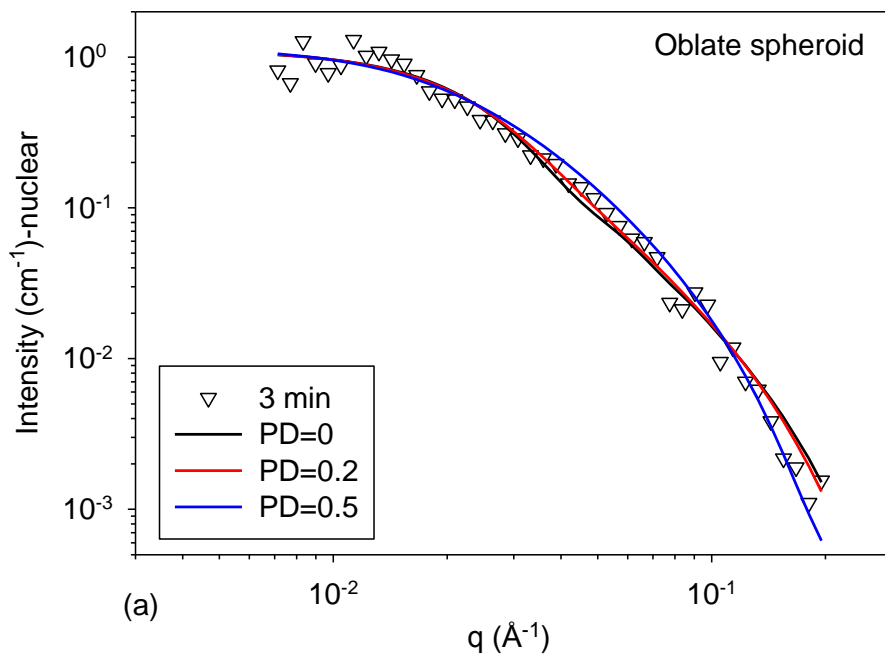
Figures SN 5.1 Experimental SANS nuclear scattering data plotted as *I versus q* from samples transformed for the time shown (symbols) along with model fitted data (solid lines) using an oblate spheroid model
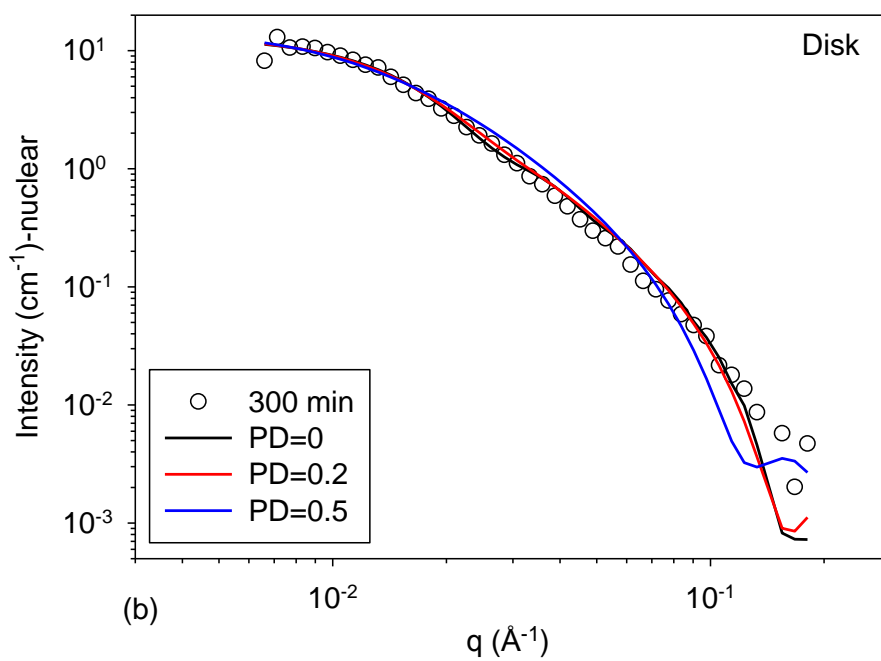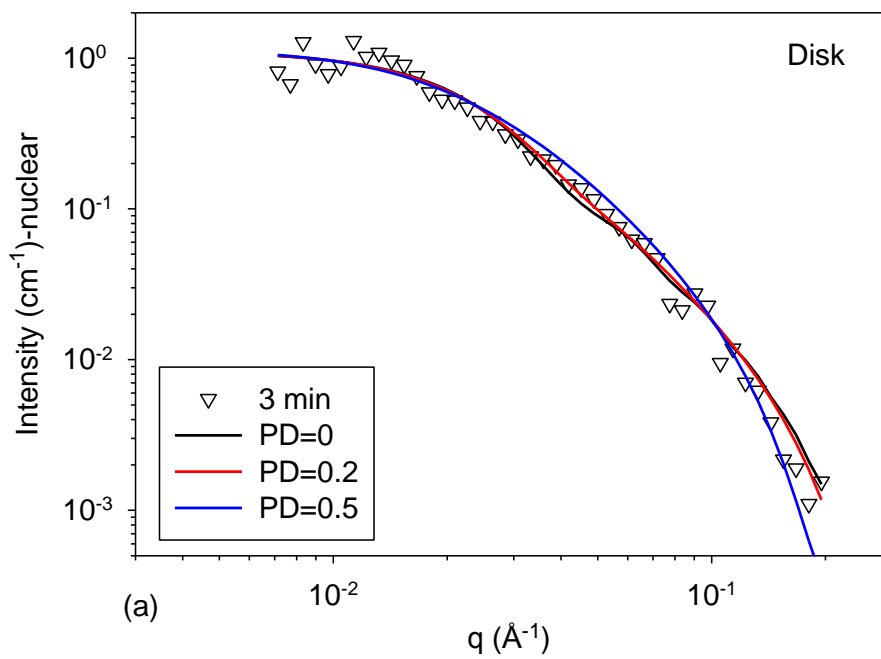
Figures SN 5.2 Experimental SANS nuclear scattering data plotted as *I versus q* from samples transformed for the time shown (symbols) along with model fitted data (solid lines) using a disc model

More detail of the fitting is given in the Tables below for the model calculations at representative ageing times and in these Tables we examine the effect of polydispersity of the major axes on the fitting for both shapes. The normalized chi-square value is computed by setting the value for the oblate spheroid calculation at $\sigma=0.5$ equal to 1. Therefore smaller normalized chi-square values equate to a better fit between model and experimental data.

Both the disc and oblate spheroid models give acceptable fitting results with very little difference between them for all ageing times but it is very clear that goodness of fit deteriorated significantly once the PD parameter exceeded 0.3. This provides justification for using a PD value of 0.2 in the representative calculations shown in the main text of the paper.

The error introduced into the estimation of equatorial radius by selecting a PD of 0.2 as opposed to 0.1 or 0.3 is of the order of ±15%. The thickness error is less than this, it is ~±10%.

AGEING TIME 3 MIN.

Dispersion parameter (PD)-equatorial radius	2 x polar radius/nm	Equatorial radius/nm	Normalised chi-square	Dispersion parameter (PD)-disc radius	Disc Thickness/nm	Disc Radius/nm	Normalised chi-square
0.1	2.5	10.2	0.909	0.1	2.1	9.1	0.908
0.2	2.7	9.1	0.921	0.2	2.3	8.1	0.920
0.3	3.0	7.5	0.947	0.3	2.5	6.7	0.947
0.4	3.3	5.9	0.982	0.4	2.8	5.2	0.982
0.5	3.7	4.4	1.000	0.5	3.2	3.9	1.000

AGEING TIME 5 MIN.

Dispersion parameter (PD)-equatorial radius	2 x polar radius/nm	Equatorial radius/nm	Normalised chi-square	Dispersion parameter (PD)-disc radius	Disc Thickness/n,m	Disc Radius/nm	Normalised chi-square
0.1	2.7	11.6	0.749	0.1	2.3	10.3	0.741
0.2	2.8	10.4	0.714	0.2	2.4	9.3	0.698
0.3	3.0	11.5	0.754	0.3	2.6	7.8	0.739
0.4	3.3	14.8	0.881	0.4	2.8	6.2	0.874
0.5	3.6	17.5	1.000	0.5	3.1	4.8	1.000

AGEING TIME 60 MIN.

Dispersion parameter (PD)-equatorial radius	2 x polar radius/nm	Equatorial radius/nm	Normalised chi-square	Dispersion parameter (PD)-disc radius	Disc Thickness/n,m	Disc Radius/nm	Normalised chi-square
0.1	3.2	12.9	0.799	0.1	2.7	11.5	0.797
0.2	3.3	11.5	0.829	0.2	2.8	10.2	0.827
0.3	3.7	9.5	0.887	0.3	3.1	8.5	0.886
0.4	4.1	7.4	0.960	0.4	3.5	6.5	0.960
0.5	4.7	5.5	1.000	0.5	4.0	4.9	1.000

AGEING TIME 300 MIN.

Dispersion parameter (PD)-equatorial radius	2 x polar radius/nm	Equatorial radius/nm	Normalised chi-square	Dispersion parameter (PD)-disc radius	Disc Thickness/n,m	Disc Radius/nm	Normalised chi-square
0.1	4.6	16.4	0.768	0.1	3.9	14.5	0.763
0.2	4.8	14.8	0.797	0.2	4.1	13.1	0.791
0.3	5.2	12.6	0.857	0.3	4.4	11.1	0.853
0.4	5.6	10.0	0.938	0.4	4.8	8.9	0.936
0.5	6.2	7.6	1.000	0.5	5.3	6.7	1.000

AGEING TIME 600 MIN.

Dispersion parameter (PD)-equatorial radius	2 x polar radius/nm	Equatorial radius/nm	Normalised chi-square	Dispersion parameter (PD)-disc radius	Disc Thickness/n,m	Disc Radius/nm	Normalised chi-square
0.1	5.9	19.4	0.665	0.1	5.0	17.2	0.659
0.2	6.2	17.5	0.714	0.2	5.3	15.5	0.708
0.3	6.7	14.8	0.805	0.3	5.7	13.1	0.801
0.4	7.3	11.8	0.918	0.4	6.2	10.4	0.917
0.5	8.1	9.0	1.000	0.5	6.9	7.9	1.000